Applications of Graphene/Fiber Heterostructures:
Portable Quantification of Mercury Ions and Vanadium Redox Flow Battery Electrodes

A Dissertation Presented for the
Doctor of Philosophy
Degree
The University of Tennessee, Knoxville

Sinchul Yeom
May 2020

Acknowledgements

Prof. Kihm is a true advisor whom I met for the first time. Without his help, I even might not be able to begin this journey again in 2015. During my Ph.D., he made every effort to support me both financially and academically. Prof. Choo, one of my committee, greatly helped me in coming to UTK, and Prof. Aaron always kindly helped in performing research and cheered me up. Prof. Shin provided warm and friendly advice during my studies. I also greatly appreciate our MABE department which allowed TA positions to me.

There are so many people in the Korean Church of Knoxville I would like to appreciate including family-like my small group members. Without my campus friends, I would have trouble in relieving my stress.

Most of all, my parents, Kapsun Yeom and Wolsuk Kim have trusted and supported me and my family all the time. My two too-lovely little boys have given me the greatest joys and meanings I can keep going. Without my wife's, Eunjeong Park's endless dedication and tears, this journey would never be ended.

Finally, I appreciate the One who has led me, loved me and given me peace and relief. I truly believe all of my journeys will work for the good in Him.

Abstract

Graphene has been considered as a wonder material since it was firstly exfoliated in 2004 due to its extraordinary intrinsic properties. Because of graphene's popularity, various types of graphene have been synthesized, and different types of graphene have their own characteristics. In this dissertation, two kinds of applications are presented using two graphene materials: graphene quantum dots (GQD) and reduced graphene oxide, respectively.

The first chapter is an introduction to the whole story. The second and the third chapters introduce two different methods for mercury ion quantification using GQDs: facile optical mercury quantification method using GQD coated filter paper disks and facile mercury ion detection method using GQD coated silica gels, respectively. The fourth chapter represents another graphene application: how can a vanadium redox flow battery's performance be enhanced using carbon-nano materials including reduced graphene oxide and xc-72 carbon nano-particles. The final chapter is the conclusion of this dissertation.

Table of Contents

List of Tables

List of Figures

Chapter 1
Introduction

In 2004, for the first time, it was experimentally proved that graphene – single atomic layer of graphite – can be separated from a bulk graphite flake and exist stably on a substrate via a very simple method called the Scotch tape method [1]. It was technically the beginning of the graphene research era, and a great number of graphene-related papers have been published since then until today, 2019. Currently, the citation number of the first graphene paper [1] is more than 45,000. What make the graphene so popular are its exceptionally outstanding properties, which were never been observed in the most of bulk materials, such as electron mobility (~ 200,000 $cm^2 V^{-1}s^{-1}$ [2]), thermal conductivity (~ 5000 W/m·K [3]), and intrinsic mechanical yield strength (130 GPa [4]). In addition, as a real two-dimensional material, it has a very high specific surface area (2630 m^2/g).

Due to graphene's popularity, various synthesis methods of the graphene materials have also been developed, and the different methods yield different sizes of graphene particles. Here, we categorize the graphene flake size in three groups: less than 30 nm (graphene quantum dot (GQD)), 1 - 15 μm (reduced graphene oxide (rGO)), and 100 μm or larger (exfoliated graphene via Scotch tape method and chemical vapor deposition (CVD) graphene). Interestingly, if graphene's size

belongs to the first size group (< 30 nm), a new quantum property appears, which is not observable in other bigger graphene materials, such as fluorescence.

My dissertation is composed of two different kinds of graphene applications utilizing the first (GQD) and the second (rGO) size groups of graphene materials, respectively, combined with fibrous materials.

The second and third chapters represent two different methods of mercury ion quantification using GQD. There have been demands for facile on-site mercury ion quantification methods in water due to its serious toxicity. GQD, fluorescent under ultra-violet (UV) light, can be easily synthesized and used as a mercury detection probe because the brightness of GQD's fluorescence decreases with the existence of mercury ions. We tried to develop simplified mercury (II) ion quantification methods using GQD coated filter paper disks in 3D-printed wells and GQD coated silica gels. For the GQD coated filter paper disks, we measured brightness by processing digital images obtained by an optical microscope. Previous works measured a change of brightness of GQD solutions in cuvettes using fluorescence spectrometer, but our method removed needs for such expensive bulky equipment and handling cuvettes, instead, it requires an image capturing device with a UV-filter and a UV light source. Our method may be easily adapted for hand-held mobile mercury detection devices in the future.

In order to overcome the limitations of filter paper method resulting from the filter paper's innate fluorescence, we used translucent silica-gel in the third chapter. We successfully synthesized silica-gels and contained GQDs in the silica-

gels, but we found it is still a long way to go in utilizing silica-gels in mercury ion quantification successfully.

The fourth chapter is about an application of reduced graphene oxide in vanadium redox flow battery (VRFB) electrodes. One of the biggest challenges of VRFBs as grid-scale batteries is high cost. As an effort for reducing the cost, we focused on enhancing the VRFBs' performance by maximizing the current density via modifications of carbon electrodes. We added pristine graphene, reduced graphene oxide film/powder, or XC-72 carbon nano-particles to carbon paper or carbon felt electrodes to increase the number of reactions sites while trying not so deteriorating mass transportation rate. The performances of VRFBs were compared at 80% voltage efficiency using polarization curves which show changes of current density depending on voltages.

Chapter 2
Portable Quantification of Mercury Ions Using Graphene Quantum Dot Coated Filter Paper

I. Introduction

There is one old report about mercury toxicity, death of the first emperor, Qin Shi Huang, of unified China by swallowing mercury pills because he believed the mercury is an elixir of the immortality [5]. However, it is not long ago that mercury poisoning has been publicly known. Mercury has been widely used in various applications such as barometer, thermometer, dental amalgams, compact fluorescent bulb (CFL), and so on, but its usages are being replaced by other materials because of mercury's toxicity. Especially for the mercury thermometer, it is around 2000s that several states of the United States started to ban sale or distribution of mercury thermometer [6]. Minamata or Chisso-Minamata disease is a well-known tragedy about methylmercury poisoning [7], a more toxic compound of mercury than mercury itself. The Chisso corporation's chemical factory in Minamata, Japan kept releasing methylmercury in their wastewater since 1932 for 36 years. People resided near Minamata Bay who consumed fish or seafood contaminated by the toxic methylmercury which was bioaccumulated via food chains were poisoned. In 2001, 2,265 of populations were officially recognized

as the victims of Minamata disease and 1,784 of them died [8]. This outbreak was mainly caused by the company executives' ignorance of methylmercury toxicity [9], and the incident became an initiator to make mercury's toxicity known worldwide.

Mercury compounds can be classified into three different forms: elemental mercury, organic mercury, and inorganic mercury. Different forms of mercury compounds have different biological behaviors and toxicity [10]. Among the various forms, methylmercury ($[CH_3Hg]^+$) is the most common form to which people are exposed and a primary cause of damaging to central nervous systems (CNS) of humans and animals [11]. A chemical precursor of the methylmercury is known as Hg^{2+} or Hg (II) ions [12], and Hg (II) is the most common oxidation state of mercury and very toxic [13]. Thus, we chose mercury (II) chloride solution as a mercury source in this work.

Because of the serious toxicity of mercury, there have been demands for facile on-site methods to measure mercury ion concentration in water. Although there have been commonly used lab-scale spectroscopies to determine mercury ion concentration of samples such as atomic absorption spectroscopy (AAS), atomic fluorescence spectroscopy (AFS), and inductively coupled plasma atomic emission spectroscopy (ICP-AES) [14], these are time-consuming, expensive, and off-site methods. To the authors' best knowledge, currently, there is no commercial on-site measurement tool to quantify mercury ion concentration in water yet. Here we report a simple optical method to measure mercury ion concentration in water which may be easily adapted for hand-held on-site mercury detection devices.

1. Graphene quantum dots

Graphene quantum dots (GQDs), nanometer-size flakes of graphene, have been spotlighted because of their easy fabrication, low cost, low toxicity and high biocompatibility, and fluorescence with high quantum yield [15-19]. GQDs have been proposed as fluorescent mercury ion detection probes in previous works because GQDs' fluorescence emission is quenched by Hg^{2+} ions with high selectivity [20, 21].

GQDs' optical properties can be modified by doping. It is known that nitrogen or sulfur doping enhances the quantum yield of graphene quantum dots [22-24]. Figure 1 (a) shows a schematic of a synthesis of nitrogen (N) and sulfur-nitrogen (SN) co-doped GQDs. N-GQD was synthesized via our previously reported IR heating method using urea and citric acid as precursors [25]. For the SN co-doped GQD, additional ammonia sulfate was used to the precursors of N-GQD. High-resolution transmission electron microscopy (HR-TEM) images of N-doped GQD and SN-doped GQD show lattice fringes of GQDs, and we can observe our GQDs have a few tens of layers.

GQD's fluorescence is mainly explained by the quantum confinement effect [26]. It is a change of electron energy levels of GQD from continuous bands to discrete energy levels because of physical confinement of electron movement in nanometer size of GQD nano-flakes. Because of the discrete electron energy levels, electrons can emit photons with a characteristic wavelength (fluorescence) under a light source (UV light).

Because physical separation of GQD nano-flakes is required for the quantum confinement to be effective, dried GQD powder which is a collection of agglomerated GQD nano-flakes is not fluorescent under UV light as shown in Figure 1 (b). There could be two methods to separate GQD nano-flakes to be fluorescent. The first method is to make a GQD dispersion by dispersing GQD powder into a solvent such as water or isopropyl alcohol. The second method is to confine GQD nano-flakes in a porous material such as filter paper. In case of the first method, when the solvent of the dispersion is dried out, GQD nano-flakes agglomerate again because of the surface tension of the solvent so they lose fluorescence again. On the other hand, in the second method case, even though the solvent of the dispersion is dried out, the GQDs in the porous material are still fluorescent because they adhere on the porous material surface rather than gathering together. GQD distributions of the dried GQD dispersion and the dried GQD coated filter paper are briefly drawn in Figure 1 (c). On the glass, GQD flakes are agglomerated and not evenly distributed, but on filter paper, GQDs adhere to fibers of filter paper without agglomeration.

We used such fluorescent dried GQD coated filter paper disks in quantifying mercury ion concentration in water. As shown in Figure 1 (b), even though the pure filter paper has its own fluorescent, the GQD coated filter paper shows brighter fluorescence, and thus we are able to utilize the phenomenon in detecting mercury ions. However, because the pure filter paper's innate fluorescent works as background noise, we need to find an optimal GQD concentration in coating filter paper disks, and this will be discussed later.

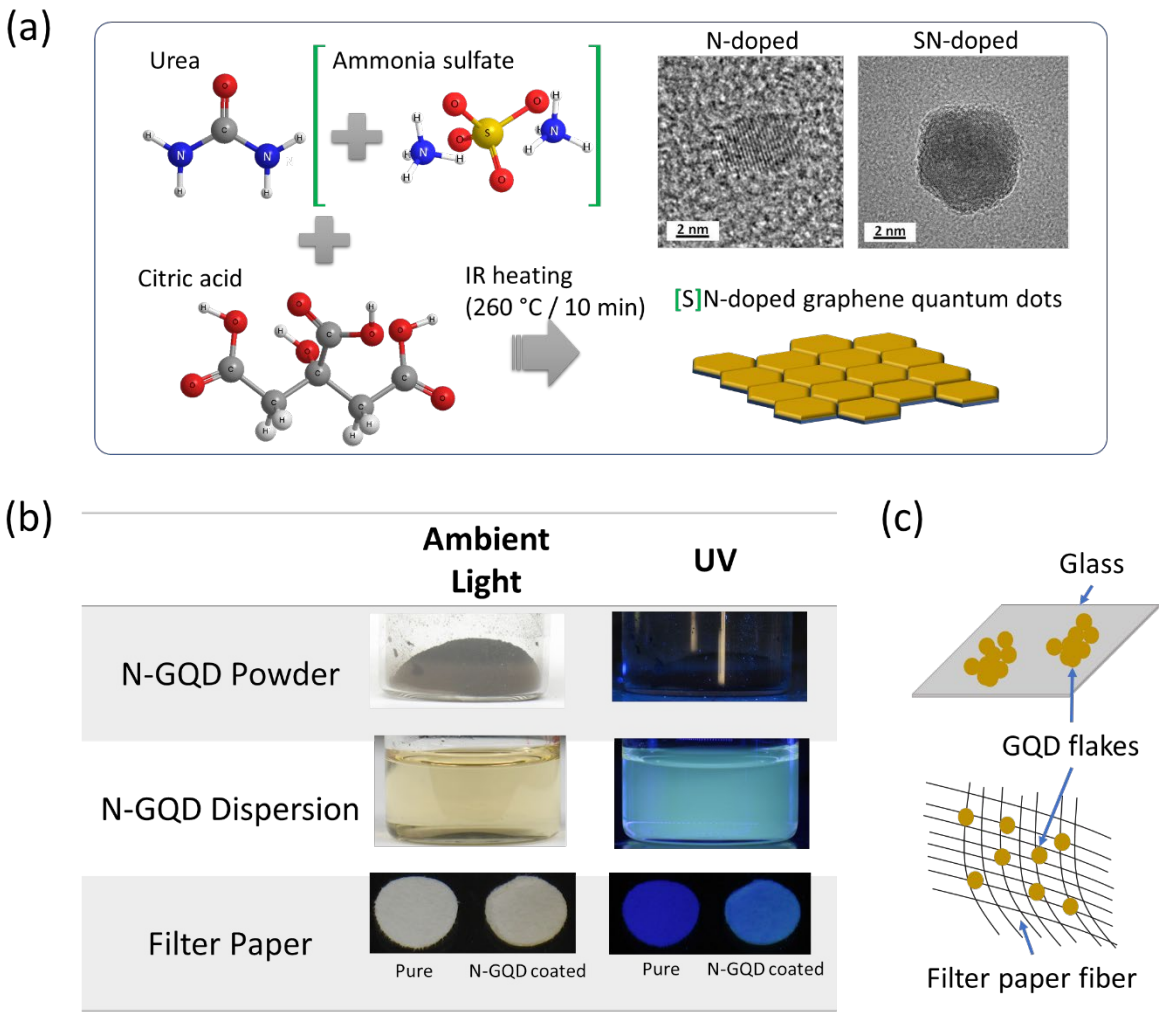

*Figure 1. (a) Synthesis of [S]N-doped graphene quantum dots. Green brackets are for SN co-doped GQDs. (inset: *HR TEM images of N-GQD and SN-GQD). (b) Digital camera images of N-GQD under different conditions (powder, water dispersion, and N-GQD coated filter paper) under ambient light vs. UV light. (c) Comparative schematic of when GQD solution droplets are dried on the glass (top) vs. on filter paper (bottom). *Attribution: Dr.Gu Siyong, Fujian Provincial Key Laboratory of Functional Materials and Applications, School of Materials Science and Engineering, Xiamen University of Technology, Xiamen 361024, China.*

2. Facile mercury quantification using GQD coated filter paper

Until now, a common way of quantifying mercury ion concentration in water using GQDs is adding sample mercury ion solutions to GQD suspensions and measuring their quenched brightness using fluorescence spectrometer or spectrofluorometer [20, 22, 25]. However, this method may not be appropriate to be applied for a portable on-site mercury detector, because GQD suspensions may need to be prepared on-site to keep the GQD suspension fresh and handling liquid in a cuvette would be bulky and inconvenient.

Thus, here we introduce a simpler method to quantify mercury ion concentration in water using GQD coated filter paper. Our method utilizes pre-prepared dried GQD coated filter paper disks. Because one disk sample's diameter is only around 6 mm, as shown in Figure 2 (b), the $31 \times 46 \times 5$ mm (7.13 cm^3) size well can hold 24 samples. Considering one standard cuvette's dimensions are $10 \times 12.5 \times 45$ mm (5.6 cm^3), used in a fluorescence spectrometer, this method achieved about 17 times more spatial efficiency regarding volume per a sample. In addition, our method requires only 45 μL of a liquid sample for one test. Also, because GQDs in the filter paper are dry, the GQDs will have a similar shelf life as raw GQD powder's. Thus, it is plausible for the method to be further developed as portable on-site devices. Although there is a report of mercury ion detection method using a paper strip coated by N and S co-doped GQD [22], the authors tried only qualitative not quantitative measurements in using the paper strip. To the best of author's knowledge, there is no report of the optical quantification method of mercury ion concentration in water using GQD coated filter paper yet.

Filter paper is one of the most ordinary porous materials, cheap, and easy to be cut and handled. We coated this normal filter paper with GQD and measured the change of quenched fluorescent brightness depending on the concentration of mercury (II) chloride solutions using microscopic images under UV light. The schematic of our method is shown in Figure 2 (a). First, we prepared sample wells using a 3D printer ((b) upper) where filter paper disks and sample solutions will be placed. Then, we pressed 1/4”-cut filter paper disks as shown in (c) using a 3D-printed press shown in (b) bottom. Then, we dropped 10 μL of a GQD dispersion in each sample well, dried the well in an oven at 50 °C, and measured before-brightness (B_0) of samples. After that, we placed 45 μL of mercury (II) chloride solution of concentration (q), dried, and measured after-brightness (B). In order to minimize sample variations, we defined each sample's intensity (I_q) at the mercury (II) chloride concentration (q) as a normalized value ($(B/B_0) \times 100$) as shown in (a).

The pressing step in our method is the most crucial finding of our report, which makes consistent contact between filter paper disk and the bottom surface of wells. Because we coated filter paper with GQD by simple drying, the GQD particles are not permanently adhered to the filter paper. Thus, when the GQD filter paper becomes wet, the adhered GQD particles are separated from the filter paper, move around, and sit back while being dried. As shown in Figure 2 (d), if the filter paper is not uniformly touched by the bottom surface, the drying liquid droplets will be gathered where the filter paper touches, and distribution of GQDs

will be uneven after dried. As a result, this uncontrolled uneven GQD distribution will cause unreliable brightness measurements. However, if we make uniform contact between the filter paper and the well using the press as shown in Figure 2 (e), the distribution of GQDs will be much evener after dried compared to the case shown in (d). Consequently, the pressing step drastically increases the reliability of measured brightness.

Figure 2 (f and g) show scanning electron microscopy (SEM) images of a pure filter paper disk, and (h and i) show a 10 μL - 200 ppm N-GQD coated filter paper disk. Due to the GQD's a few nanometer-scale sizes, GQD looking like small particles are not observable via SEM. As shown in Figure 2 (j), we also tried to find GQD peaks from the N-GQD coated filter paper using Raman spectrometer. Pure GQD powder shows two peaks around 1500 cm^{-1}, but the filter paper disk coated by very high concentration (200 ppm) of N-GQD dispersion does not show much different spectrum from regular filter paper disk's. It is because the amount of coated GQD is not enough to be detected by Raman spectroscopy.

In this work, we quantitatively measured the change of fluorescent brightness depending on mercury (II) chloride concentration using GQD coated filter paper disks via optical microscopy.

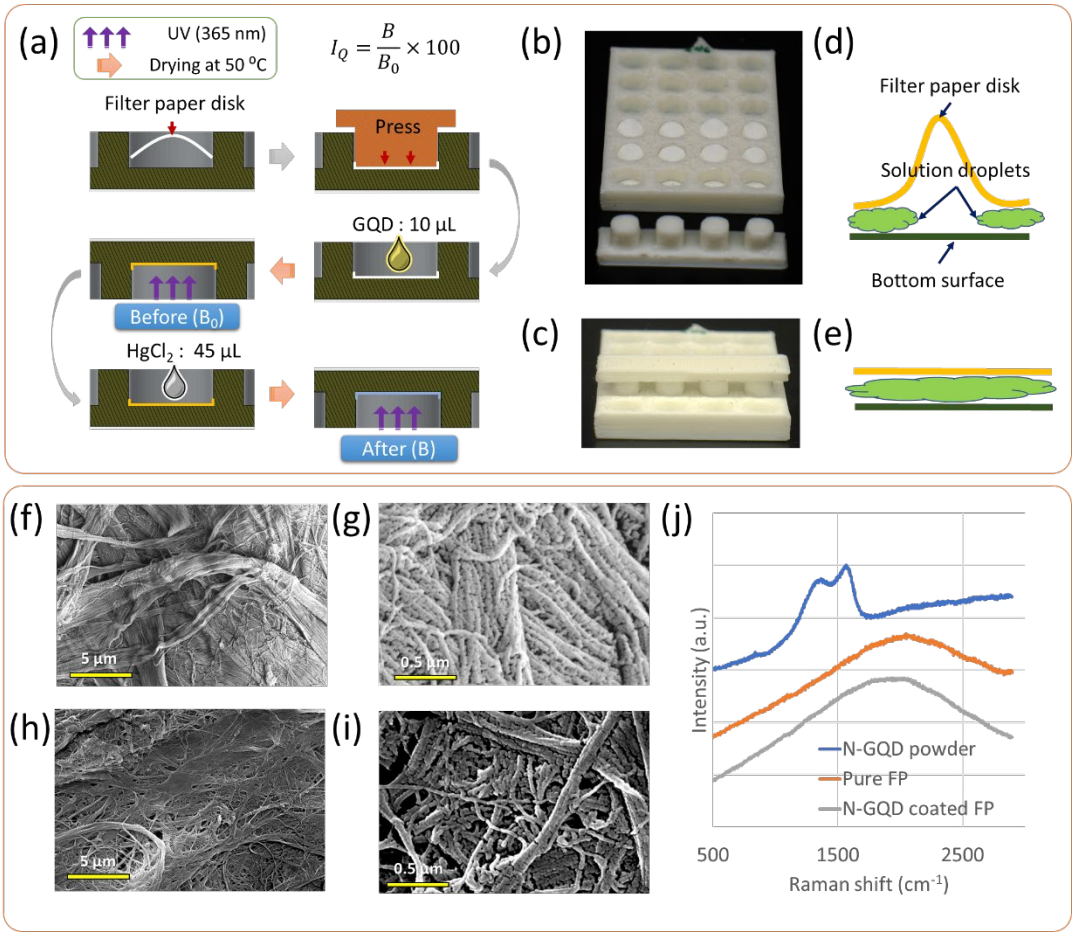

*Figure 2. (a) Schematic of a facile mercury ion quantification method. The intensity, I_Q, at the mercury (II) chloride concentration, Q, is defined as the normalized value, $(B/B_0) \times 100$. (b) Test wells (top) and press (bottom). The well's dimensions are $31 \times 46 \times 5$ mm. (c) When filter paper is pressed by the press. (d and e) Comparative schematics of when the filter paper (d) is not pressed and (e) is pressed showing solution distribution when dried out. *(f-i) SEM images of (f and g) pure filter paper and (h and i) 10 µL 200 ppm N-GQD coated filter paper. (j) Raman spectrum of N-GQD powder, pure filter paper, and 10 µL 200 ppm N-GQD coated filter paper. *Attribution: Department of Chemical Engineering and Materials Science, Yuan Ze University, Taoyuan 32003, Taiwan.*

II. **Experimental**

1. GQD powder and dispersions

N-doped GQD powder was synthesized via previously reported infrared (IR) assisted pyrolysis method [25], and the schematic of the synthesis is shown in Figure 1(a). Briefly, citric acid and urea in 2:1 weight ratio were blended by a 3-D mixer using Zr balls, and the mixture was heated in IR furnace at 260 °C for 10 min. After cooled down, the N-GQD was scraped and sieved. For the SN-GQD synthesis, ammonia sulfate was added to the N-GQD's precursors, and the weight ratio of citric acid, urea, and the ammonia sulfate was 1:1:1. The following steps were same as N-GQD's. GQD dispersions were prepared mostly by two-step dilutions. For example, for a 5 ppm GQD dispersion, first, a 200 ppm of GQD dispersion was prepared by dispersing 4 mg of GQD in 19.996 g of DI water and sonicating it for 30 min. Next, 0.4 g of 200 ppm dispersion was mixed with 15.6 g of DI water to be diluted as 5 ppm dispersion.

2. Mercury (II) chloride solutions

Mercury chloride solutions were prepared by multi-step dilutions. First, a 2000 ppm solution was prepared by dissolving 40 mg of purchased mercury (II) chloride powder (Fischer scientific, 99.5%) in 19.96 g of DI water. The 2000 ppm solution was diluted to 500 ppm, and then, the 500 ppm was diluted to 50 ppm. 2, 4, 6, 8, and 10 ppm solutions were prepared using the same 50 ppm solution. Sub ppm solutions were diluted from the 10 ppm solution. All solutions were weighted on Ohaus PA 84 analytical balance whose minimum readability is 0.1 mg.

3. Test well and press

Test well and the press were designed using OpenSCAD software and 3D-printed. The diameter of each well is determined as 5.8 mm which is slightly smaller than filter paper disk's (1/4" = 6.35 mm) to be tightly fitted when the paper disk is pressed. The depth of the well is determined as 4.5 mm to be able to hold 45 µL of liquid while minimizing printing time. Raise3D™ Pro2 Plus was used to print the test well and the press using Raise3D™ Premium PLA filament. Standard-setting with 100% infill density was used for printing, and other settings were adjusted to remove any gaps on the bottom surface.

4. Sample preparation and acquisition of fluorescent images

The schematic of this method is shown in Figure 2 (a). Whatman qualitative filter paper (1005-090, 9 cm dia., and 2.5 µm pore size) was cut into 1/4" dia. disks using a paper punch. The disks were placed in the 3-D printed 5.8 mm dia. wells and pressed by the 3-D printed 5.6 mm dia. press to ensure uniform contact with the bottom surface of the wells. To coat the filter paper disks, a 10 µL of GQD dispersion was pipetted onto each seated filter paper disk in the well, and the disks were dried in an oven at 50 °C. Then, their fluorescent microscopic images were taken to measure before-reference-brightness (B_0). To measure quenched brightness, 45 µL of a Q concentration of mercury (II) chloride solution was pipetted onto the prepared GQD-coated disk placed in the test well, the disk was dried in the oven at 50 °C, and again fluorescent microscopic images were taken to measure the quenched after-brightness (B). Each sample's normalized intensity, I_Q, at the mercury (II) chloride concentration, Q was calculated as $(B/B_0) \times 100$.

5. Brightness measurement

The brightness of each sample was calculated from each microscopic image. OSRAM HBO 100W/2 mercury lamp was used as a light source, and Olympus U-MNU2 filter cube whose excitation filter's wavelength range is 360-370 nm was used. The images were captured via a 4x microscope objectives by OMax A35180U3 digital camera under 365 nm UV light with a fixed exposure time. The exposure time was determined to maximize average brightness while each maximum value of each color channel (red (R), green (G), and blue (B)) does not exceed maximum pixel value (255) to avoid saturation. All images' resolution is 4912 by 3684 pixels, and the center circular area with the radius of 1500 pixels was chosen and averaged. The averages of pixel's R, G, and B values were combined and converted to an averaged greyscale value using a formula, 0.299R + 0.587G + 0.114B, defined in ITU Recommendation BT. 601-7 [27], and the converted greyscale value is used as a brightness value. The calculation process was automated by a python script.

III. **Results and discussion**

1. Fluorescent intensity vs. mercury (II) chloride concentration

Figure 3 (a) shows a schematic of the fluorescence imaging process of a sample using an inverted microscope, Olympus IX71. Our test well was turned over for the inverted microscope, and a mercury lamp whose light spectrum includes both visible light and UV light was used as the light source. The excitation-filter

filters 365 nm UV light, and the UV light is reflected by the dichroic mirror towards the objective lens and shines the sample. Then, rays including both the fluorescent visible spectrum from the sample and the reflected UV spectrum go back to the objective, and the visible rays longer than 400 nm pass through the dichroic mirror. Visible rays longer than 420 nm are filtered by the emission filter and reach the camera. This fluorescence image is captured by the digital camera and the brightness is obtained from the image.

Figure 3 (b) shows one of fluorescence sample images used for before-brightness (B_0) at each mercury (II) chloride concentration, and (c) shows each corresponding quenched fluorescent image used for after brightness (B). For better reliability, having similar brightness values for (b) is desirable, and we can qualitatively observe overall brightness of (b) look similar to each other. On the other hands, Figure 3 (c) images show a gradual decrease of brightness with increasing [$HgCl_2$], and the quantitative change of normalized intensities are shown in the graph (d).

The quenching mechanism of GQD's fluorescence by mercury (II) ions is known as complex formation of GQD-$(Hg^{2+})_x$ on the GQD surface [25]. The formed complex hinders photon emission from excited electrons by blocking direct jump from the lowest unoccupied molecular orbital (LUMO) to the highest occupied molecular orbitals (HOMO) [25]. The reason for the slope becomes less steep over the 6 ppm in Figure 3 (d) may be explained by a decrease in the complex formation rate. If the formation rate is constant regardless of the [$HgCl_2$], the slope in (d) would be also constant provided the brightness is proportional to the number

of GQD flakes which did not form complexes. However, if the rate is reduced as the [$HgCl_2$] increases, the slope in the graph (d) is expected to be gradual.

We can observe quite descent linear relationship between mercury (II) chloride concentration and the normalized quenched intensity up to the 6 ppm in the graph (d). Each intensity value is the average of five sample values, and the standard errors of the sample variations range from ±0.53 to ±1.27. The error bars in the graph (d) indicate averaged standard errors of spatial brightness variations which are mainly due to randomly distributed fibers in filter paper disks. We can observe several relatively dark spots in Figure 3 (b and c) images, which are one of the reasons for error bars of the graph (d). Our result shows a reliable relationship between 0 and 10 ppm $HgCl_2$ solution ranges even though such innate filter paper's variations exist, and from this graph, we will be able to identify a concentration of an unknown mercury ion solution.

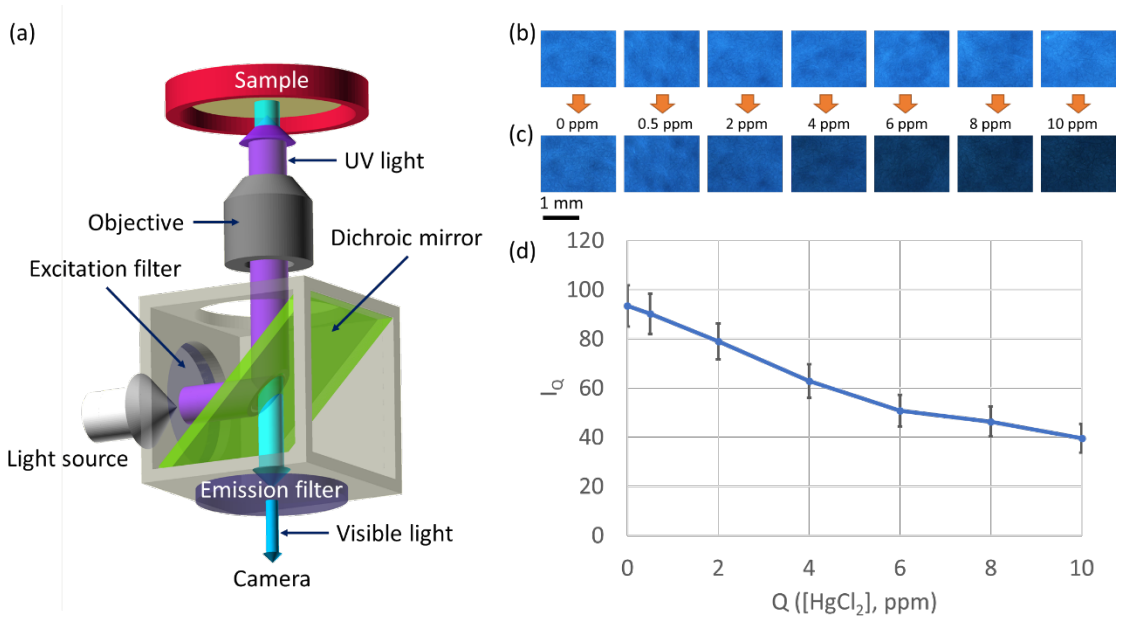

Figure 3. (a) Schematic of the fluorescence imaging process of a GQD-coated sample via Olympus® U-MNU2 mirror unit. The light source is Osram HBO 100W/2 mercury lamp. (b-c) Microscopic fluorescent images of N-GQD coated filter paper disks (b) before and (c) after quenched by mercury (II) chloride solutions of different concentrations under UV light. All images' scale bar is the same. (d) Quenched fluorescence intensity of 10 µL - 5 ppm N-GQD coated filter paper disks (I_Q) at different [$HgCl_2$], Q. Each data point is an average of five sample values, and the error bars indicate averaged standard errors of areal intensity variations.

2. GQD concentration vs. sensitivity

Fluorescent intensity of a GQD dispersion under UV light is proportional to its concentration. More fluorescent GQD nano-flakes means more brightness, and this is also applied to the GQD coated filter paper disks. In coating filter paper disks, if we use more amount of GQD nano-flakes, we could obtain brighter fluorescent GQD filter papers. Because filter paper has its innate fluorescence (background noise) as shown in Figure 1 (b), brighter GQD fluorescence will make itself more distinctive from the innate filter paper's. However, in order to detect the lower concentration of $HgCl_2$ ions, fewer number of GQD nano-flakes is desirable. It is because greater number of GQD nano-flakes requires the greater number of mercury ions to observe the same degree of change of fluorescent quenching effect.

Figure 4 (a) shows the difference in mercury detection sensitivity depending on the concentration of N-GQD dispersion. For the 10 ppm N-GQD dispersions, we can observe the brightness decreases roughly to a half when mixed with a 20 ppm $HgCl_2$ solution, and it loses its most of fluorescence with a 100 ppm $HgCl_2$ solution. However, for the 1000 ppm solutions, the brightness looks not changing at all even mixed with a 100 ppm $HgCl_2$ solution. Figure 4 (b) is a schematic explaining the effect of N-GQD concentration on mercury detection sensitivity. If we assume one GQD diagram corresponds to 5 ppm GQD nano-flakes in a 0.5 g GQD dispersion, the 10 ppm dispersion will have 2 GQD diagrams, and the 1000 ppm dispersion will have 200 GQD diagrams. If fluorescent brightness of the dispersion is proportional to only the number of GQD nano-flakes, initial intensity (I_0) ratio of the 10 vs. 1000 ppm dispersions would be 2:200. Also, if we assume

that a 0.5 g 20 ppm $HgCl_2$ solution quenches exactly one GQD diagram (5 ppm), fluorescence intensity change ratios (I_0:I) of 10 and 1000 ppm dispersions would be 2:1 and 200:199, respectively. In other words, for the 10 ppm GQD, a 20 ppm $HgCl_2$ solution quenches 50 % of the initial fluorescence, but for the 1000 ppm GQD, only 0.5 % of the initial intensity decreases. Therefore, regarding detection sensitivity, less amount of GQD is better.

Although Figure 4 (a and b) are about GQD dispersions, we would expect the same tendency may apply to our developed method which utilized GQD coated filter paper disks. Figure 4 (c) shows this relation between sensitivity and GQD amount in filter paper disks. We tested the dependency of mercury detection sensitivity on GQD amount of filter paper disks following the schematic of Figure 2 (a). The GQD amount was controlled by changing the concentration of a dispersion while maintaining the volume of the dispersion as same as in the schematic, 10 μL. The graphs in (c) show intensities normalized by their I_0, where only D.I. water is used for the quenching test.

For the 1 ppm case, where the minimum amount of GQD was used, if there is no filter paper's innate fluorescence, the 1 ppm would be the most sensitive case. However, the actual 1 ppm case show the least change of intensity at even the 100 ppm [$HgCl_2$]. It is because the brightness of GQD coated filter paper is only slightly greater than innate filter paper's due to too little GQD amount, thus, the quenched brightness is not much different from the initial brightness I_0. In other words, if we lower the GQD amount too much, then we will also have lower sensitive result because of filter paper's fluorescence.

After several trials and errors, we found the 5 ppm of GQD gives the best sensitive result in our method, and the 5 ppm graph shows the steepest change of the intensity especially in the low [$HgCl_2$] range among the graphs of (c). As explained, because the 5 ppm is the most sensitive case here, we may expect that an increase in GQD concentration from 5 ppm may lower the detection sensitivity (the slope became gradual). The 100 ppm case shows this prediction compared to 25 and 5 ppm case, but the slope of 25 ppm is not much different from 5 ppm's from 2 to 6 ppm of [$HgCl_2$]. However, for the 25 ppm GQD, in 0 – 2 ppm of [$HgCl_2$] range, the brightness looks jittering around 1 rather than decreasing steadily because 25 ppm GQD is too much to show discernible brightness changes by 0-2 ppm $HgCl_2$ solutions. To sum up, though the 25 ppm GQD shows similar slope to 5 ppm's in 2-6 ppm [$HgCl_2$] range, considering the 25 ppm GQD is not able to detect 0-2 ppm [$HgCl_2$], the 5 ppm GQD would be the most sensitive condition in our method.

(a)

[N-GQD] \ [$HgCl_2$]	0	2	10	20	100
10	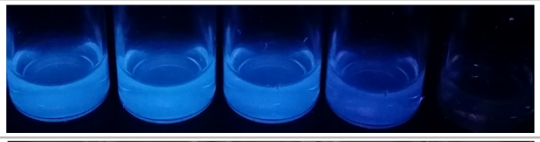				
1000	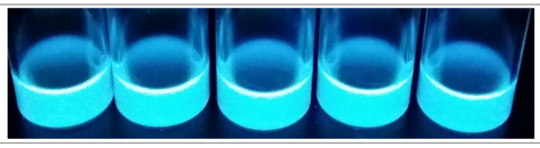				

(b)

[N-GQD]	Fluorescent N-GQD flakes	I_0:I
10		2:1
1000	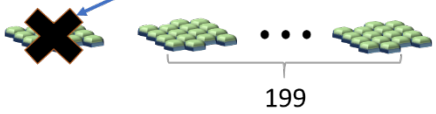	200:199

(c)

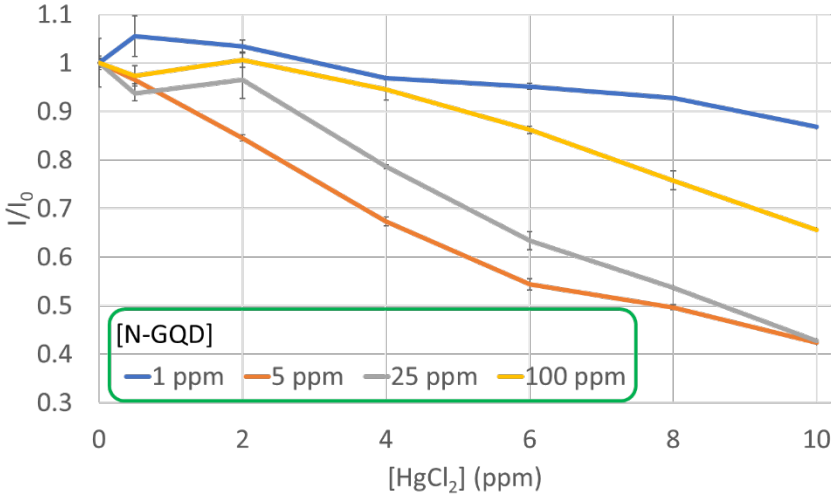

Figure 4. GQD concentration and mercury ion detection sensitivity. Concentration units are ppm. (a) Digital camera images showing mixtures of 0.5 g N-GQD solutions and 0.5 g mercury (II) chloride solutions of different concentrations under UV light. (b) Schematic explaining the difference of quenched fluorescence intensity depending on N-GQD concentrations when quenched by a 0.5 g 20 ppm $HgCl_2$ solution. One GQD diagram corresponds to 5 ppm in a 0.5 g N-GQD solution, and X mark corresponds to a 0.5 g 20 ppm $HgCl_2$ solution. (c) Various normalized quenched fluorescence intensity changes depending on [$HgCl_2$], and concentration of 10 µL N-GQD solutions used for filter paper coating varies from 1 ppm to 100 ppm. Error bars indicate standard errors of sample variations.

3. N-GQD vs. SN-GQD

One of the advantages of GQD is its properties can be easily tuned by doping. It is known that nitrogen and sulfur co-doping enhances not only its quantum yield but also mercury detection sensitivity, and it is previously reported that SN-GQD dispersion is more sensitive than N-GQD dispersion in detecting mercury ions in water [25]. It is because SN-GQD has C-SOx-C (x=2,3, and 4) sulfone bridges, and the bridges allow more mercury ions to adhere to the SN-GQD surface [25]. It means the SN-GQD forms SN-GQD and mercury ion complexes more easily than N-GQD.

We compared how do N-GQD and SN-GQD behave differently in our developed method. Figure 5 shows normalized intensity changes of N-GQD and SN-GQD coated filter paper disks when GQD dispersions of different concentrations were used. As explained in the previous sections, more sensitivity means more rapid decrease of normalized intensity with the increase of [$HgCl_2$]. In Figure 5, concentrations of the same color graphs were determined to have roughly similar before-brightness under similar exposure time. The reason for about 15 times higher concentration of SN-GQD dispersion is low dispersibility of our SN-GQD powder. The SN-GQD powder was not fully dispersed as the N-GQD powder did while making the dispersion even we sonicated it more than an hour, so, presented concentrations were simply calculated based on weights of mixed SN-GQD powder and water. Thus, actual concentrations of SN-GQD dispersions would be lower than the calculated values. However, because all the SN-GQD dispersions were diluted from one 200 ppm SN-GQD dispersion, concentration

ratios between dispersions are accurate though we do not know actual concentrations of SN-GQD dispersions.

Figure 5 (a) shows normalized quenched fluorescence intensity when [$HgCl_2$] ranges from 0 to 8 ppm. For the SN-GQD, the intensity drops more rapidly in 0 – 0.5 ppm than N-GQD's, but its slope became less steep than N-GQD's as the [$HgCl_2$] increases. The 100 ppm SN-GQD is not an optimal (most sensitive) concentration yet, because in (b), slopes still become steeper (increasing sensitivity) as SN-GQD concentration increases until 150 ppm. Thus, even though 100 ppm SN-GQD is not the most sensitive case, in 0-0.5 ppm [$HgCl_2$] range, SN-GQD looks slightly more sensitive than N-GQD.

Figure 5 (b) shows other test results under lower [$HgCl_2$] range, 0-1.6 ppm. For N-GQD, all three graphs do not show any distinctive relationships between [$HgCl_2$] and the intensity, even for the 3 ppm case which is nearly same as the N-GQD's optimal concentration, 5 ppm. Normalized intensities are jitters around 1, and it means under these test conditions, 0-1.6 ppm of $HgCl_2$ solutions are difficult to be detected. However, for the SN-GQD, the graphs show relatively stable and steady decrease in the intensity with the increase in [$HgCl_2$] from 0.4 ppm. Also, the graphs show the effect of SN-GQD concentration on the mercury detection sensitivity, i.e., as SN-GQD concentration increases, the slopes of the graphs become steeper. Thus, SN-GQD may be used to detect 0.4-1.6 ppm of $HgCl_2$ solutions in our method, but N-GQD is not appropriate for the range.

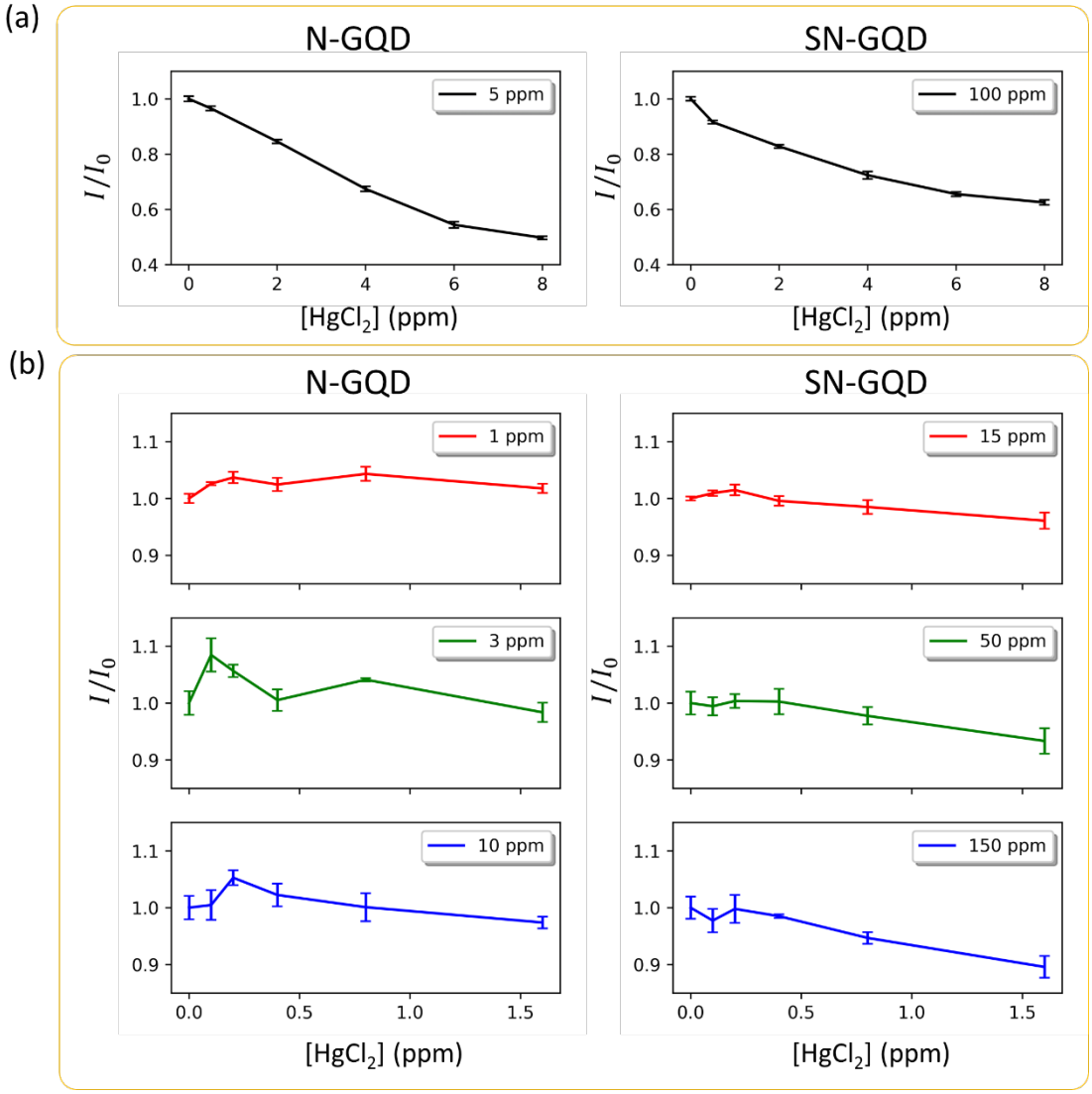

Figure 5. Comparisons of N-GQD and SN-GQD in our developed mercury quantification method. Legends indicate concentrations of 10 µL GQD solutions used in coating filter paper disks, and error bars are standard errors of sample variations. (a) When $HgCl_2$ concentration ranges from 0 to 8 ppm. (b) When $HgCl_2$ concentration ranges from 0 to 1.6 ppm.

IV. **Conclusion**

We developed a facile optical method to quantify mercury ion concentration in water using GQD coated filter paper disks in 3D-printed wells and an optical microscope. Our method is cost-effective, the test kit occupies small volume, only 45 μL of a liquid sample is necessary for one test, and because of its simplicity, the method may be easily applied to a portable mercury detection device. Using our method, we obtained the fluorescence intensity vs. [$HgCl_2$] curve, and it can be used to calculate an unknown mercury solution's concentration. Detection sensitivity is highly dependent on the concentration of GQD solutions used for coating filter paper disks, and the 5 ppm 10 μL N-GQD solution showed the best mercury detection sensitivity in 0-6 ppm mercury (II) chloride solution range. SN-GQD solution is known to have better sensitivity than N-GQD, and the dried SN-GQD used in our method also showed better mercury detection sensitivity than N-GQD in 0.4-1.6 ppm of $HgCl_2$ concentration range.

Chapter 3
Portable Quantification of Mercury Ions Using Silica Gel

I. Introduction

Silica-gel is a type of desiccant commonly used in our everyday lives. Silica-gel is literally a gel made of silica, which is called quarts and also a main ingredient of glass. Silica gel's technical name is silica-xerogel, which means it is made by being dried from silica-liquid gels such as silica-hydrogel, silica-alcogel, and so on ('xero' means 'dry' in Greek). While silica-xerogel is being made, liquid molecules in silica-liquid gels leave nanopores during evaporation, thus the silica-liquid gel becomes nano-porous silica gel after dried.

Because silica (quartz) is transparent, a porous translucent silica-gel could be one of the best candidates for holding GQDs inside while observable from outside. Although the 2-D filter paper method is quite successful, the method has a detection limit due to inherent fluorescence of the filter paper itself. We noted that translucent and porous silica gel does not have such inherent fluorescence, thus, using silica gels may lower the detection limit of mercury ions. In this work, we tried to develop a method to measure mercury ion concentration using GQD contained-Si-gels.

1. Synthesis of silica xerogel

Silica gel has a relatively old history. Its first discovery is known as early as 1640 [28], and its synthesis method was patented by professor Walter A. Patrick in 1919 [29]. In synthesizing silica gel, common precursors are known as tetraethyl orthosilicate (TEOS, $Si(OC_2H_5)_4$), tetramethyl orthosilicate (TMOS, $Si(OCH_3)_4$), and sodium silicate (water glass, $(Na_2O)_x \cdot SiO_2$) [30]. Among these, we chose one type of sodium silicate, sodium metasilicate (Na_2SiO_3) as our precursor for silica gel synthesis, because it is the cheapest material among three and requires only a common acid or a base as an additional ingredient for the synthesis.

The first step of the silica gel synthesis is synthesis of silica hydrogel. Silica hydrogel is made via sol-gel process, and the first reaction is neutralizing sodium metasilicate by hydrochloric acid to produce silicic acid ($Si(OH)_4$) as in the following reaction [30]:

$$Na_2SiO_3 + H_2O + 2HCl \rightarrow Si(OH)_4 + 2NaCl.$$

Then the silicic acid sequentially forms silica particles, chains, and network structures (silica hydrogel) as in the following reaction [30]:

$$n[Si(OH)_4 + (OH)_4Si] \rightarrow n\left[\begin{array}{cccc} & OH & OH & \\ & | & | & \\ OH- & Si & -O- & Si-OH \\ & | & | & \\ & OH & OH & \end{array}\right] + 2nH_2O.$$

There are several parameters which affect sol-gel reaction of the silicic acid solution: concentration, temperature, pH, and any additives used [30]. Silica hydrogel can also be formed by using a base instead of an acid, and it is known the

pH value of the mixed solution greatly affects the final form of silica [30]. If the pH level is low (acidic), silica particles form liner chains rather than cross linked structures, so the formed silica become relatively soft [30]. If the pH level is high (basic), silica become relatively hard because more branched networks are formed than linear chains [30].

Because silica is very brittle, if we place commercial silica gels in water, we can easily observe they are shattered because of the strong capillary force due to a few nanometer-size pores of silica gels. In quantifying mercury ion concentration, it is desirable that the silica gel, as a GQD's container, keeps its own shape rather than being shattered in water. Thus, in our work, we only used hydrochloric acid for the silica gel synthesis in order to minimize chances to be cracked by making it softer.

Once the silica hydrogel is formed, the next step is to rinse salts (NaCl in our work) in silica hydrogel out which were formed in the very first step, neutralization. If the salts remain in the hydrogel, when the hydrogel is being dried, the crystalized salts break the internal structures of the silica gel, and we obtain only shattered glass powder as a final product instead of silica gel.

The last step is to remove water from the silica hydrogel. There are several ways to remove water from the hydrogel, and the different ways of drying produce different types of porous silica such as silica aerogel and silica xerogel. In order to make silica xerogel, we can simply dry the silica hydrogel in air or in oven to reduce time. While the silica hydrogel is being dried, it shrinks quite a lot, more than 60%

of its original length because of water's high surface tension. When we need less shrunk silica xerogel, replacing the water in hydrogel before dried with some other solvents whose surface tensions are lower than the water's is helpful in reducing shrinkage of the silica xerogel.

2. Synthesis of GQD contained silica xerogel

Figure 6 shows a schematic of synthesis of both regular Si-xerogel and GQD contained Si-xerogel. Following steps of a, b, c, and I, produces regular silica xerogel, and additional processes are necessary to place GQD inside Si-xerogel. There could be three places where additional steps could be inserted in Figure 6, and they are a, c, and I.

First, we tried to mix GQD in the step a with silica acid solution to contain GQD in Si-xerogel, but it turned out that GQD's color is kind of bleached by the silicic acid. Also, as mentioned in the previous section, because salts in Si-hydrogel need to be rinsed out, if GQD is mixed in Si-hydrogel before being rinsed, most of

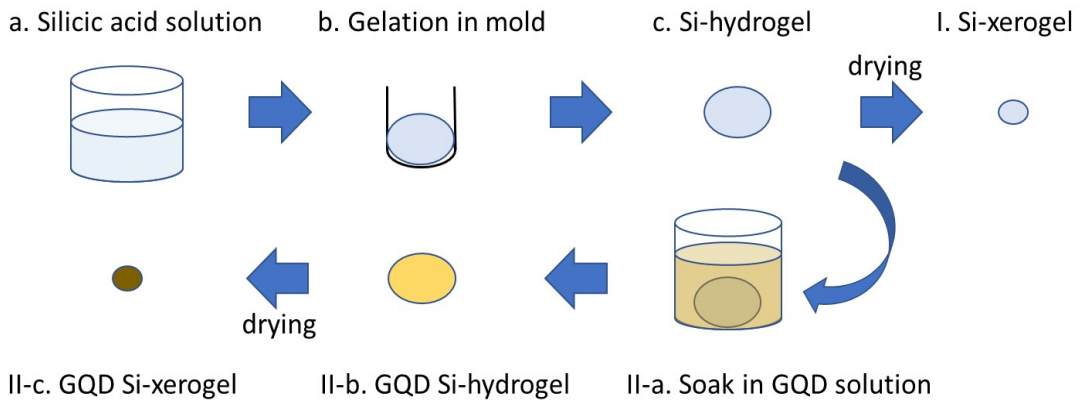

Figure 6. Schematic showing synthesis of both regular silica xerogel (a, b, c, and I) and GQD silica xerogel (a, b, c, II-a, II-b, and II-c).

the GQD would also be rinsed out with salts while being rinsed. Thus, mixing GQD in the early stage (step a) is not a good idea.

If we add GQD to Si-xerogel in step I in Figure 6 by soaking dried Si-gel into a GQD solution and drying the Si-gel, it would be the simplest way to contain GQD in Si-xerogel. However, because there is nothing physically or chemically holding GQD inside silica gel, if we wet the Si-gel to do a mercury quenching test, GQD inside Si-gel will be easily dissolved out and it will be difficult to quantify mercury ion concentration.

Thus, we chose the step c in Figure 6 in adding GQD to Si-xerogel. By simply replacing water in Si-hydrogel with GQD solution via diffusion, GQD can be placed inside the Si-hydrogel. Also, because Si-hydrogel shrinks a lot during drying process, we can expect GQD molecules may be physically held by interconnected silica nets if we are able to control shrunk pore size to be slightly less than GQD molecule's size.

II. **Initial approach**

One important prerequisite of successful quantification of mercury ions is how to accurately control the amount of mercury ions and GQD in quenching reaction. Because we use silica gel as a container for GQD, first, we need to control the amount of GQD in each silica gels, and then controlled amount of mercury ions should react with GQD in silica gel.

Two factors which determine the amount of GQD in silica gel are the volume of silica hydrogel and concentration of a GQD solution where the silica hydrogel is soaked. The volume of silica hydrogel is determined by the volume of a silica acid solution which can be easily and accurately controlled using an adjustable pipette, and so does the concentration of a GQD solution. However, controlling the amount of mercury ions to be reacted with GQD in silica gel is quite challenging. At the first time, we considered placing GQD contained silica gel in a known concentration of mercury ion solution, but it turned out the GQD in the silica gel started to be dissolved out once the GQD-silica-gel was placed in the mercury ion solution. Thus, instead of placing silica gel in a solution, we decided to make a certain amount of mercury ion solution be fully absorbed by the GQD-silica-gel.

We devised a method to keep a constant number of mercury ions touching GQD-silica-gel by changing the shape of the silica gel as shown in Figure 7. In the

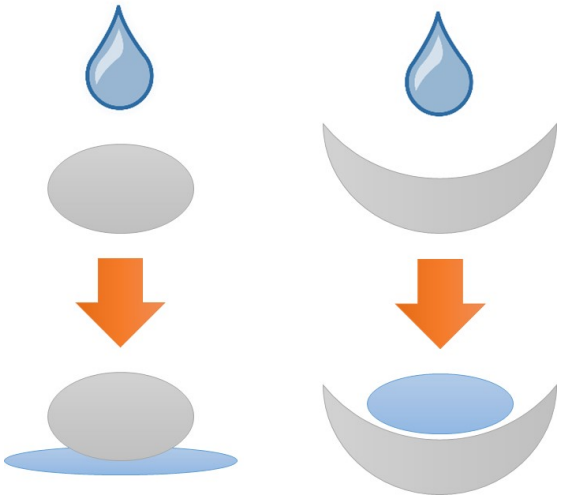

Figure 7. Comparative cross-sectional view of dropping a mercury solution (light blue) on different shapes of silica gels (grey): conventional spherical shape (left side) and devised bowl shape (right side).

figure, the left side indicates when we drop a mercury solution droplet on a conventional spherical silica gel, and we can expect the solution will instantly spill along the surface to the bottom of the silica gel. However, if we can make a silica gel like a bowl shown in the right side of Figure 7, a measured volume of a mercury ion solution will be kept inside of the silica gel bowl rather than spilled out.

We designed a bowl-shaped mold as shown in Figure 8. Considering silica gel is very brittle, surface of the mold should be as smooth as possible. Also, in order to make more room for mercury solution, a bowl needs to be as deep as possible. Figure 8-a shows the result of our efforts to satisfy these criteria, and the curve was mathematically drawn by an elaborately determined cubic polynomial function. The silica hydrogel and silica xerogel in Figure 8-d were synthesized following the schematic of Figure 6 using the 3D-printed bowl-shaped mold shown in Figure 8-c.

We could successfully obtain the silica gel bowl, but the bowl idea did not work well contrary to our expectation. Most of all, the bowl-shaped silica gel is more easily cracked than spherical ones. One of the reasons for more fragility could be that the surface of the 3D-printed mold is not enough smooth as our design because of physical resolution limit of a 3D-printer we used. Besides, the bowl we finally obtained (xerogel) was too small for a practical experiment. It was extremally difficult to drop a smallest drop on the Si-xerogel bowl shown in Figure 8-d (left top) whose outside diameter is around 4 mm. Even a really tiny drop of a solution (2 uL) was spilled over out of the bowl. We may increase the mold size to make the Si-gel bowl bigger, but usually bigger silica gel is more easily shattered

than small ones once water is absorbed. Thus, we stopped our first attempt here, and tried to find another method in quantifying mercury ion concentration using GQD contained silica gels.

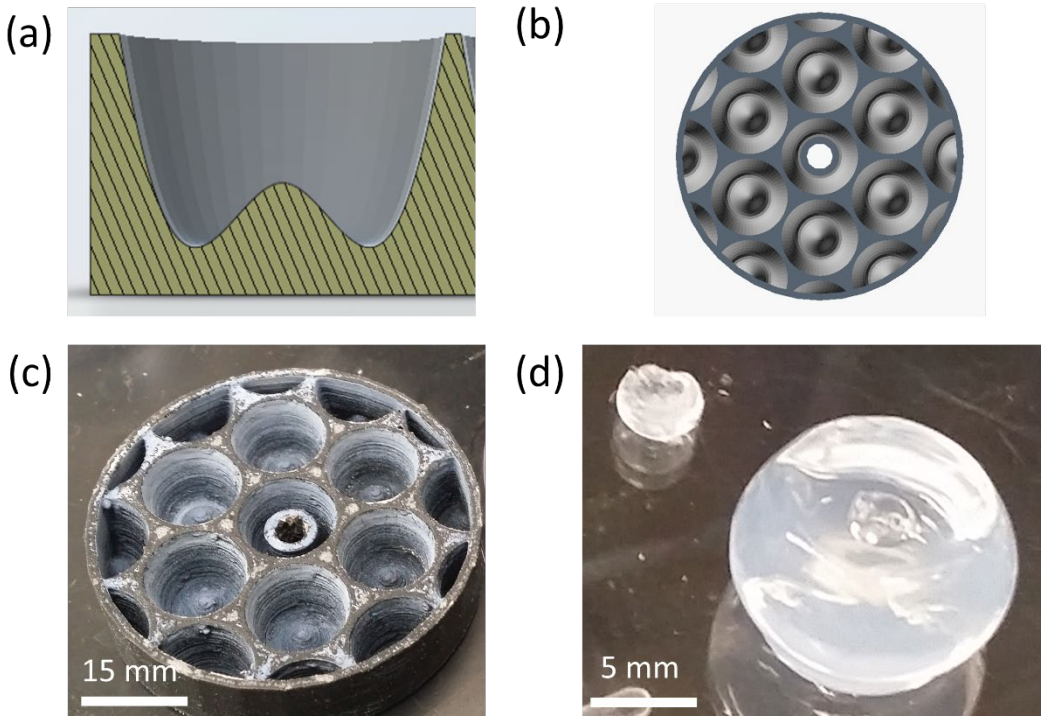

Figure 8. (a-c) Mold for bowl-shaped silica gel: (a) cross sectional view of one of the six molds, (b) top view, and (c) 3D-printed mold (white color surface is due to superhydrophobic coating). (d) Bowl-shaped silica xerogel (let-top) and hydrogel (right-bottom).

III. **Second approach**

Synthesis of GQD contained silica gels can be simply done by placing silica hydrogels in a GQD solution and drying the GQD contained hydrogels as described in Figure 6. Despite this method's simplicity, the downside is that the GQDs inside the silica gels are not firmly adhered. In other worlds, as soon as the GQD contained silica gels are placed in water, the GQD flakes are dispersed out, and that makes quantification of mercury ions almost impossible.

In this approach, we focus on holding GQD flakes inside silica gels using a polymer which may work as an adhesive between GQD and silica gels. Once GQD stays inside silica gels even when the silica gels are placed in water, we may be able to find a minimal quenchable mercury ion concentration for a GQD silica gel as described in Figure 9. The goal of this approach is development of GQD silica gels which has a certain value (Q) of minimum quenchable mercury ion concentration. Provided GQD remains in silica gel when placed in water, we can assume GQD silica gels made by a process batch may have the same number of GQD flakes during mercury quenching test. In order to quench a certain number of GQD flakes,

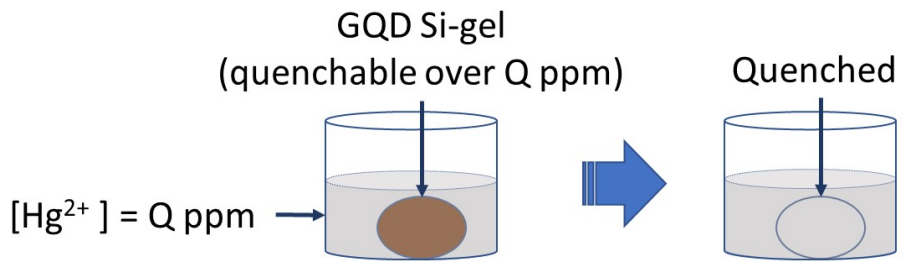

Figure 9. Schematic showing GQD silica gel which is quenchable in Q ppm mercury ion solution under UV light.

there needs to be a certain number of mercury ions, and that may mean there exists a minimum quenchable concentration Q for the GQD silica gels.

If we could successfully develop such a GQD silica gel whose minimal quenchable concentration is Q, such silica gel may be used to quantify mercury ion concentration in water as shown in Figure 10. Different types of GQD contained silica gels will be prepared, and each silica gel will have its own minimum quenchable concentration such as 1, 10, or 100 ppm. The prepared different GQD silica gels will be dropped into a mercury solution of unknown concentration, and which Si-gels are quenched will be identified. The concentration will be determined as a range from the maximum quenched Si-gel's ppm (10 ppm in the example) to the minimum not-quenched Si-gel's ppm (100 ppm in the example).

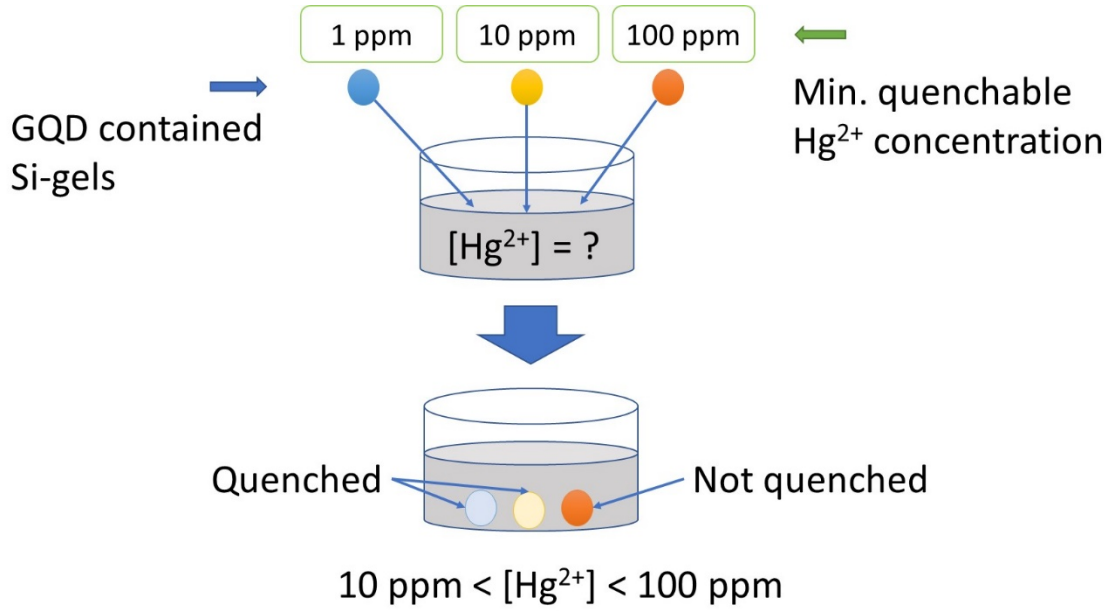

Figure 10. An example of mercury ion concentration measurement using three different GQD contained silica gels which have their own minimal quenchable mercury ion concentrations such as 1, 10, and 100 ppm.

Thus, the measured concentration will be 10 – 100 ppm in the example shown in Figure 10.

1. Nafion™

Nafion™ is a trademark of a copolymer of tetrafluoroethylene (Teflon®) and perfluoro-3,6-dioxa-4-methyl-7-octene-sulfonic acid. Simply speaking, Nafion™ has a Teflon® backbone whose some of side chains are another fluorocarbons, and the side chains have a sulfonic acid (-SO_3H) terminal [31]. Nafion membrane has been used as a proton pass membrane in various types of batteries. Nafion's backbone, Teflon, is hydrophobic and Nafion's terminal, the sulfonic acid, is hydrophilic. Because of this amibiphilic property of the Nafion, we decided to use the Nafion as an additive to hold GQD in silica gel. We used Nafion 117 solution ~5% in a mixture of lower aliphatic alcohols and water in synthesizing GQD contained silica gels.

2. Methodology

GQD-Nafion Si-gel is prepared as shown in Figure 11, slightly modified from the schematic in Figure 6. The first step is to make a precursor, silicic acid solution, which will become silica hydrogel, by neutralizing hydrochloric acid with a slightly basic sodium silicate solution. In preparing the silicic acid solution (step a), first, we made a 10 wt% sodium silicate solution by dissolving sodium metasilicate powder (Anhydrous, technical grade, Alfa Aesar) in DI water. Because we need silicic acid of low pH value, we dropped the sodium silicate solution in the hydrochloric acid (HCl). If we mix the other way (dropping HCl in the sodium silicate solution), the mixed solution becomes gelated before reaching the targeted

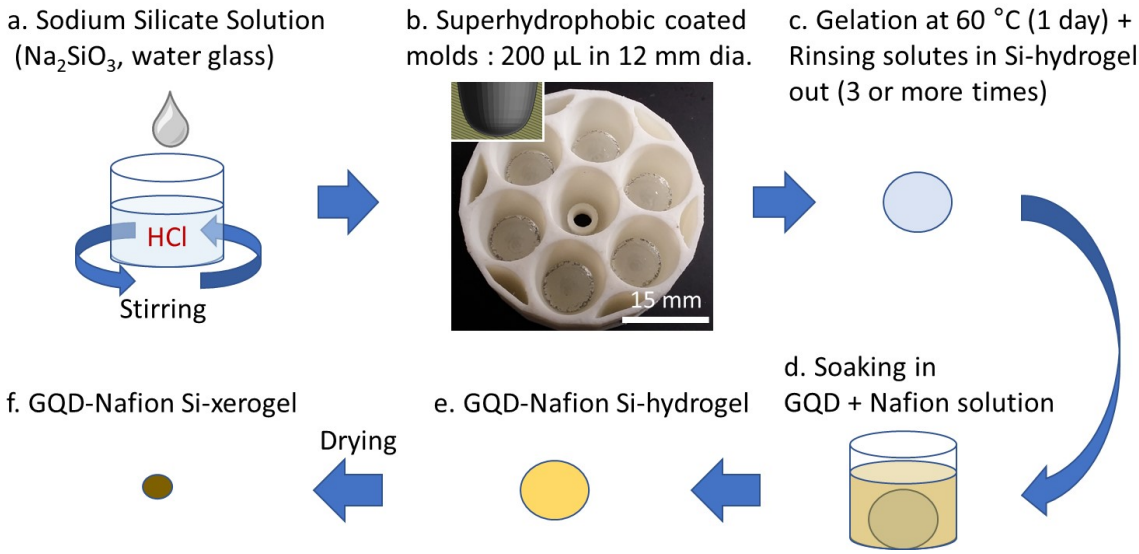

Figure 11. Synthesis of GQD-Nafion silica xerogel. In step b, the inset shows a cross sectional view of one of molds.

pH value. Mixing sodium silicate solution in HCl requires a great care, because the silicic acid's property is greatly dependent on its pH value and the pH value is quite tricky to be controlled without any buffer solution. Also, it is very import to stir the solution well during the entire mixing process especially near the end of the process, otherwise tiny silica particles can be formed instantly when a HCl droplet added to the solution. We added the 10 wt% sodium silicate solution to the 32 wt% hydrochloric acid (ACS grade, Amazon.com), and the molar ratio of HCl to sodium silicate was empirically determined as around 2.32 to 1 which corresponds to 1 g of 32 wt% HCl solution to 4.62 g of 10 wt% sodium silicate solution. For the accurate measurement, we used a 0.1 mg resolution scale to measure weights of solutions and solutes instead of measuring volumetrically. The 2.32 molar ratio was determined solely by gelation time which shouldn't be too long or too short, so we could have enough time to place the solution in the mold. Slightly decreasing the

molar ratio such as 2.1 makes gelation instant, and the slightly increasing the ratio makes the gelation time too long like more than a few days. In order to reduce the gelation time after the solution is placed in the molds, we placed the solution in 50 °C oven to accelerate the reaction.

In designing molds, we tried to make moderately flat sphere. If the mold is too deep, there is a high chance that hydrogel is stuck in the mold after gelation. For the structural stability, perfect sphere would be the best, but because it requires a quite complicated process to be made, we chose an oblate spheroid as our silica gel shape. The mold was designed using OpenSCAD software to easily adjust mold parameters such as radius and height, and it was printed by a 3D-printer, Raise3D Pro2Plus. In order to make surface as smooth as possible while keeping printing time not so long, we chose the high-quality printing option (0.1 mm layer height) and 100% infill-density. After the mold was printed out, oozed surface was smoothed out using a tweezer, and the surface was coated with Rust-Oleum Neverwet Multi-surface sprays. The Neverwet spray is for superhydrophobic coating which prevents the synthesized hydrogel from being stuck in the mold, and it helps silica hydrogel's surface to be smoother by preventing the silicic acid solution from wetting the mold.

The superhydrophobic coating is basically a two-step process. The first step is base coating which covers surface with some elastic polymer which helps better adhesion between top-coat and the target surface. Figure 12 shows molds right after the base-coat was sprayed. After the base coating is fully dried, the top- coat

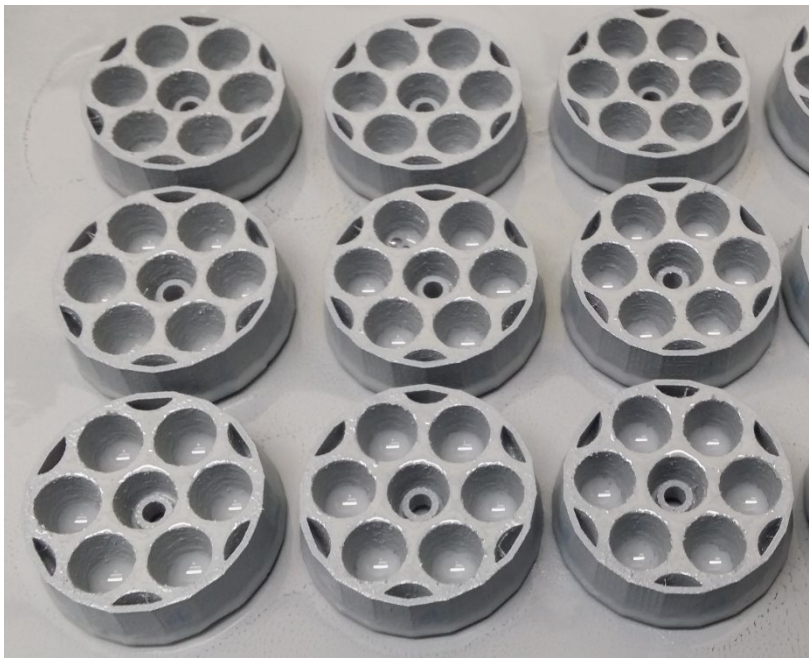

Figure 12. Base coating step of superhydrophobic coating for silica gel molds.

is sprayed, which is superhydrophobic powder. Because our purpose is preventing hydrogel from sticking to the surface, the top-coat needs to be fully covered without leaving any tiny spots uncovered. Thus, several times of thin coating is preferred. Once the top-coat is fully dried, the molds need to be rinsed by water to remove not-adhered white superhydrophobic powder, otherwise those powders will be floating around on silicic acid solution in the molds. Also, during rinsing, it is recommended to check any water droplets remain on the superhydrophobic coated surface.

Once the molds are prepared, 200 μL of the prepared silicic acid is piped into each mold whose diameter is 12 mm. The molds filled with the precursor are kept at 50 °C for one day in a glass container with a twisted top in order for the silica acid not to be dried out before being gelated. The gelated hydrogels are

carefully separated from the molds by slightly shaking upside down on a DI water bath. And, the solutes inside the hydrogels are rinsed out by submerging the Si-hydrogels in a clean DI water bath, waiting for about an hour until the solutes are moved out by diffusion, replacing the water by clean DI water, and repeating the process three or more times. Then, the rinsed Si-hydrogels are soaked in a GQD-Nafion solution and left for three hours until GQD-Nafion molecules are placed inside by diffusion. Finally, the GQD-Nafion Si-hydrogels are dried to become GQD-Nafion Si-xerogels.

Figure 13 shows xerogelation of N-GQD contained silica hydrogels, and different concentration of N-GQD solutions were used. As we can expect, a higher concentration of GQD contained silica gel show brighter fluorescence under UV light. Once a hydrogel becomes a xerogel, its diameter shrinks to approximately one third of its hydrogel's diameter. Interesting thing is the 166 ppm-xerogel's fluorescence brightness: it is less bright than even 20 ppm-xerogel's. It may be explained that distances between GQD flakes become too close because of too much GQD flakes in the silica xerogel. So, the GQD's quantum confinement effect which requires physical separation of GQD flakes is no longer valid.

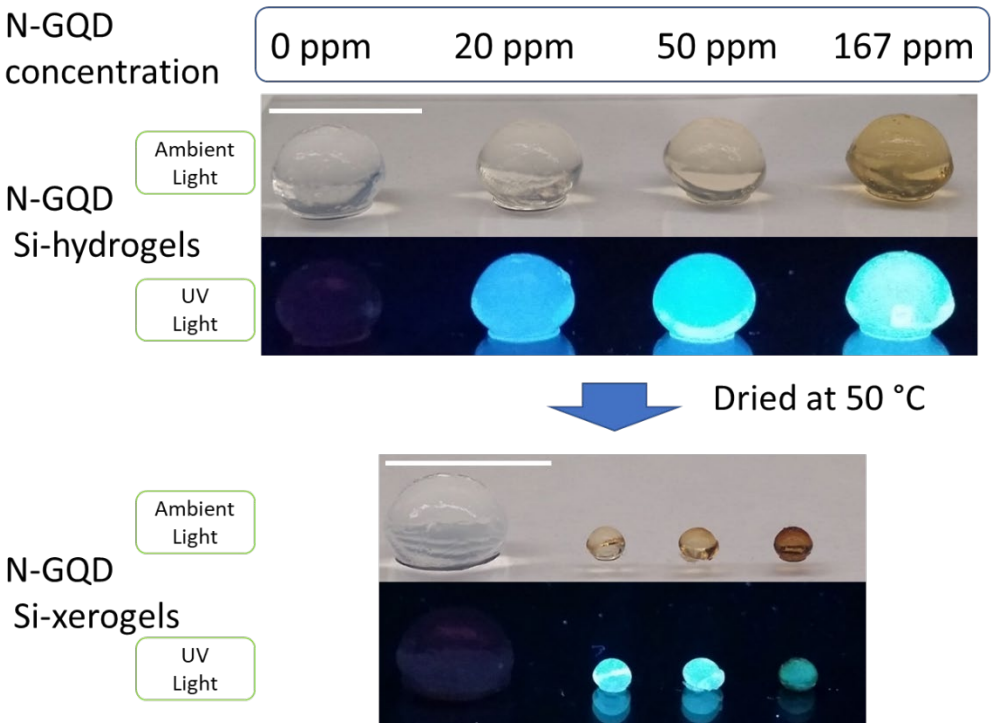

Figure 13. Xerogelation of (a) N-GQD contained silica hydrogel. Different concentration of N-GQD solutions were used. In (b), the left most is the same 0 ppm silica hydrogel of (a). Scale bars are 15 mm.

3. Test

As shown in Figure 14, we prepared two different samples (i and ii) to verify whether Nafion effectively can hold GQD flakes inside, and we performed two different tests (a and b) using these two different samples to see whether mercury ions can reach inside the silica gels and quench GQD's fluorescence. In preparing the sample (i), we mixed 3 mL of 50 ppm N-GQD solution with 2 mL of DI water for the soaking solution shown in Figure 11-d, and for the sample (ii), we used 3 mL of 50 ppm N-GQD solution mixed with 2 mL of 200 ppm Nafion 117 solution. Because our Nafion solution is 5 wt% which corresponds to 50000 ppm, we diluted the original Nafion solution by DI water to prepare 200 ppm solution. Only difference between the sample (i) and (ii) is whether they include Nafion in silica gels or not, thus, if Nafion works as an adhesive, GQD flakes in silica gels would not or less be desorbed out during test. Also, we compared how does GQD silica gels fluorescence change in (a) water and (b) mercury ion solution.

Figure 14 shows time lapse of fluorescence images under UV light of four different cases. The pictures were taken by Canon A640 digital camera, and locations of light source, the camera, and the samples were fixed in order to observe fluorescence brightness changes solely by desorption of GQD flakes or mercury quenching without any other environmental brightness changes. Also, we tried to fix exposure time for the most of cases to compare brightness intuitively without additional brightness adjustment.

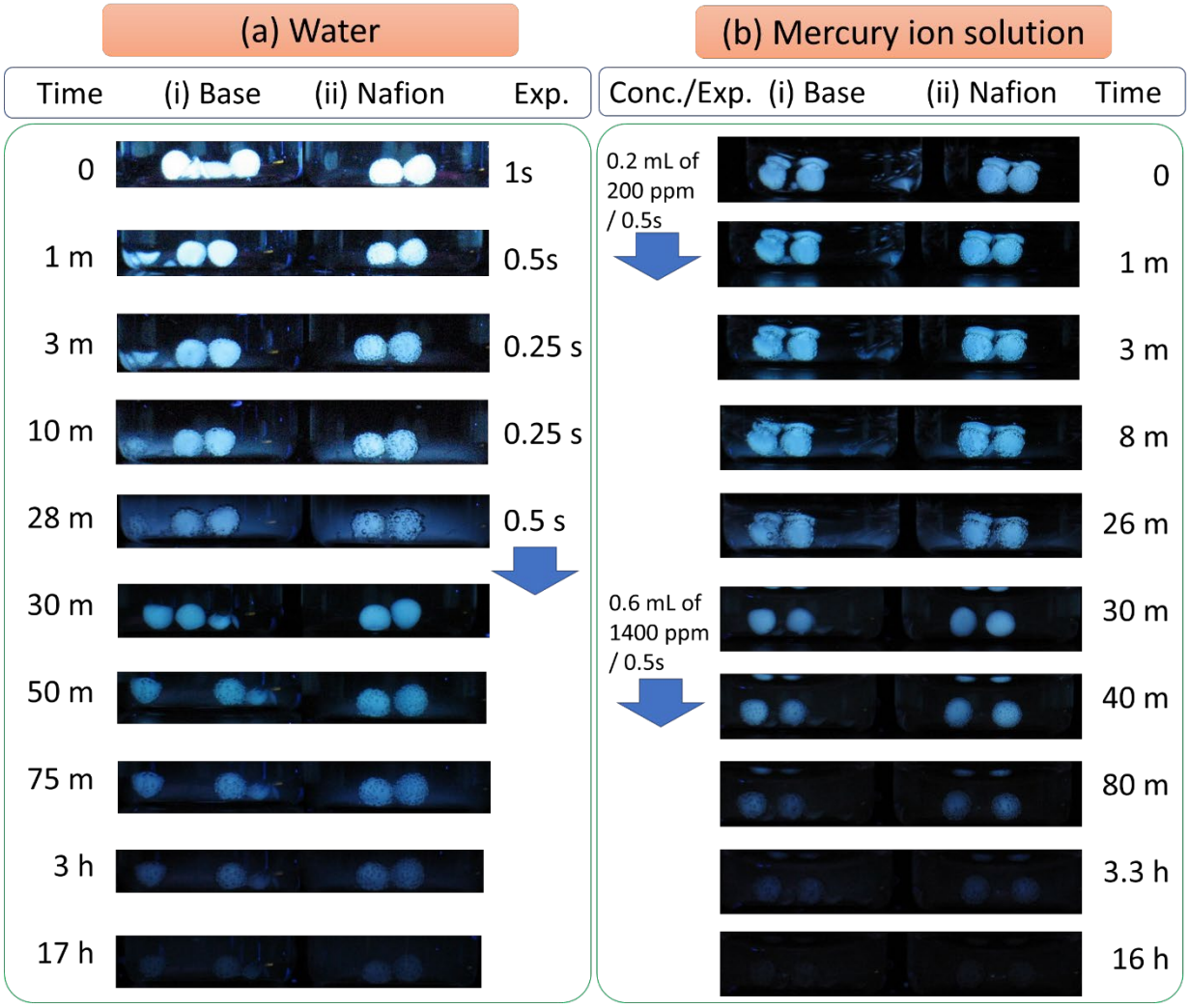

Figure 14. Time lapse of fluorescence of two different silica gels, (i) base and (ii) Nafion in (a) water and (b) mercury ion solution.

IV. **Result and discussion**

In Figure 14, we compared effect of Nafion (i and ii) on GQD molecule desorption in both cases (a and b), and unfortunately, there is no discernable brightness difference between (i) and (ii) in both (a) and (b) regardless of the time lapse. In Figure 14-a, at 28 min, the brightness significantly decreases compared to at 1 min's, and GQD flakes desorbed out of the silica gels are observable looking like cloud around the silica gels. The Nafion did not hold GQD flakes, and at 17 hr in Figure 14-a, fluorescence of silica gels is almost not observable in the 0.5 s exposed picture.

Quenching effect by mercury ions can be observed by comparing (a) and (b) in Figure 14 (either (i) or (ii)). In most of time we can observe (b) is slightly less bright than (a) and it is quite distinctive at 1 min. However, instant (or a short time) quenching effect, which is more desirable, is not observable in (b). It looks GQD flakes near silica gel's surface are quenched instantly by comparing the pictures of (a) and (b) at 1 min, but the brightness looks not decreasing much for the first 30 mins in (b). It may be explained mercury ions cannot or take long to reach inside of silica gels because of dense and interconnected silica gel's structure. Particle size of our GQD flakes are known as 3 - 5 nm [25], and a mercury (II) ion's diameter is known as 0.23 nm [32] which is about one twentieth of GQD molecule's. Because the GQDs inside of silica gels are able to be desorbed out, much smaller mercury (II) ions may also be able to diffuse into silica gels. However, considering GQD quenching reaction by mercury happens almost instantly, brightness decreases in (b) would be mainly due to the desorption of GQDs from silica gels. In (b) at 30

min, we increased the concentration of mercury ion solution to 1400 ppm by adding 0.4 mL of 2000 ppm solution to the initial 0.2 mL of 200 ppm solution expecting to see faster quenching effect. However, increased mercury ion solution still did not effectively quench the GQD silica gels even after 10 mins passed. For the (b), it took about 3.3 hours to lose the most of fluorescence in the 0.5 s exposed picture.

To sum up, in this test, we added Nafion as an adhesive to GQD solution expecting to delay or stop the desorption of GQD flakes from silica gels, but the Nafion did not make any distinctive effect on the result. Secondly, we expected fluorescence of GQD silica gels to be quenched in mercury ion solutions in a short time, but the decrease of fluorescence brightness was mostly due to the desorption of GQD flakes rather than mercury quenching.

V. **Conclusion**

We tried our effort to develop a method to quantify mercury ions in water using GQD contained silica gels, but we still have a long way to go. In our first approach, we made bowl-shaped silica gels to keep a certain amount of mercury ion solutions to be contacted with GQDs, but we stopped our effort because of inherently extremely fragile silica gels when wet. We may continue this approach if we could solve the shattering problem of silica gels when wet. In the second approach, we set a goal to synthesize GQD silica gels which have a certain minimum quenchable mercury ion concentration, Q, so the silica gels' fluorescence

can be quenched in a short time in a Q concentration of mercury ion solution. We tried Nafion as an adhesive to hold GQD flakes inside silica gels, but it turned out the Nafion did not work as an adhesive in our test condition. Also, we test mercury ion quenching effect to GQD silica gels, but, unfortunately, the mercury could not effectively quench GQD inside of the silica gels. In order to continue our journey, we would need to find an adhesive which can hold GQD flakes inside of silica gels and a way to increase quenching speed so we can detect change of brightness distinctively with naked eyes.

Chapter 4
Reduced Graphene Oxide in Vanadium Redox Flow Battery (VRFB) Electrodes [33][1]

I. Preface

As a grid-scale electrical energy storage (EES) system, redox flow batteries (RFBs) have drawn many researchers' attention over the last 10 years [34] due to their independent energy capacity scaling from power, low maintenance cost, and geographical insensitivity. Among various RFBs, all vanadium redox flow batteries (VRFBs) are mostly investigated, and a general schematic and layers of a VRFB are shown in Figure 15-a and c, respectively. The current biggest hurdle in scaling the VRFBs up is the high cost of membrane material and vanadium. Thus, many research works have been focused on reducing the membrane and redox material cost [35]. However, the total system cost per KW-h also can be reduced by increasing the current density or power density.

We tried to maximize the electrical current density of VRFB by modifying carbon electrodes using various carbon materials. The current density of the battery is proportional to mass transportation rate of ions through electrodes and

[1] This chapter includes a published work. From Chapter 4-II, the same copy of the published work, "Kinetic enhancement via passive deposition of carbon-based nanomaterials in vanadium redox flow batteries." is included.

the number of reactions sites in the electrodes. However, usually, mass transportation rate and the number of reaction sites cannot be increased at the same time, because in a fixed volume, more reaction sites mean more amount of electrode materials, and that inherently reduces the mass transportation rate.

Three different classes of carbon nanoparticles were added to conventional VRFB electrode materials in this work: (1) pristine CVD graphene, (2) reduced graphene oxide (rGO) flakes, and (3) XC-72R carbon nanoparticles, and two kinds of electrode materials were used: (a) carbon paper and (b) carbon felt. Among the eight test conditions in Table 1, we observed three successful enhancement conditions marked in blue.

In this work, performances of different setups of VRFBs were compared using polarization curves as shown in Figure 17, Figure 18, and Figure 19. A polarization curve shows changes in current density (mA/cm^2) while increasing (charging) or decreasing (discharging) the applied voltage (V) of a battery. The voltage efficiency is defined as $V_{discharge}/V_{charge}$, and the 75-80% voltage efficiency is considered as industrial-accepted. In interpreting the polarization curves, better performance means that a battery can flow more current at the same voltage efficiency. In other words, the more a curve bends towards inside, the more current flows at the same voltage efficiency, which means better performance. The curves in Figure 17 (c) show a slight performance improvement at the 80% voltage efficiency when rGO film was added to a carbon paper electrode (●) compared to a plain paper electrode (■).

II. Introduction

Redox flow batteries (RFBs) are positioned to be a leading technology for grid-scale energy storage due to their independent energy and power capacity scaling, geographical insensitivity, and projected durability. The primary barrier to their widespread implementation is cost, which can be surmounted via inexpensive materials or by improved performance. Current efforts in redox flow battery research span from investigations of organic and aqueous redox systems to development of higher performance materials (especially membranes and electrodes). Most current commercial systems are based on the all-vanadium redox chemistry. In this paper, significantly increased operating current with industry-accepted voltage efficiency (75 - 80%) is demonstrated via a technique that can be applied to new systems or readily retrofitted to existing flow battery stacks. With any performance improvement claim, durability must be considered as well. Because the method presented in this work uses graphitized carbon and no reliance on functional groups or other catalysts, durability is expected to be on-par with the base electrodes used in flow batteries. Additionally, the nature of this system modification lends itself to facile maintenance should electrode loss be observed over the industry-expected 10,000 – 20,000 cycle lifetime.

1. Vanadium redox flow batteries (VRFBs)

Redox flow batteries have matured considerably over the past 10 years of research and burgeoning industrial development [34]. The potential for these devices to enable a renewable energy-based grid by moderating output between variable energy sources and the grid provides the impetus for such growth.

Advantages including rapid dispatchability, independent power and energy capacity scaling, long lifetime with low maintenance requirements, and operational flexibility position RFBs as choice electrical energy storage systems [36]. Other energy storage technologies, including Li-based batteries, pumped hydroelectric, and compressed air, have limitations that can be avoided with RFBs at similar costs [37]. Of the many chemistries considered for RFBs, all-vanadium redox flow batteries are the most widely-produced and investigated, with more than a dozen companies currently producing them on the kW/kW-hr or greater scale. A general schematic of a VRFB is included in Figure 15-a. The cost of VRFBs has been predicted by multiple research groups, including analyses of which components most strongly influence cost [38-41]. Of the numerous contributors to system cost, membrane material and vanadium often make up nearly two thirds of total system cost. Thus, many current research and development efforts are aimed at exploring lower-cost membrane materials and/or redox chemistries [35]. An equally viable option for significant cost reduction, however, is increasing the current density or power density at some acceptable voltage or voltage efficiency, often close to 80%, while accessing a suitable state of charge (SOC) window to more fully utilize the vanadium capacity [42].

Increases in system performance generally focus on improved redox kinetics via greater surface area or more active electrode materials [43-48], the use of thinner or more proton-permeable membranes [49-51], and improved mass transport through the electrode structures [47]. Each of these avenues targets particular overpotentials present in all electrochemical systems [52]. Given the

general preference for relatively lower current that enables higher voltage efficiency operations, improved electrode structures and materials offer a promising route to cost reduction by allowing greater power density stacks.

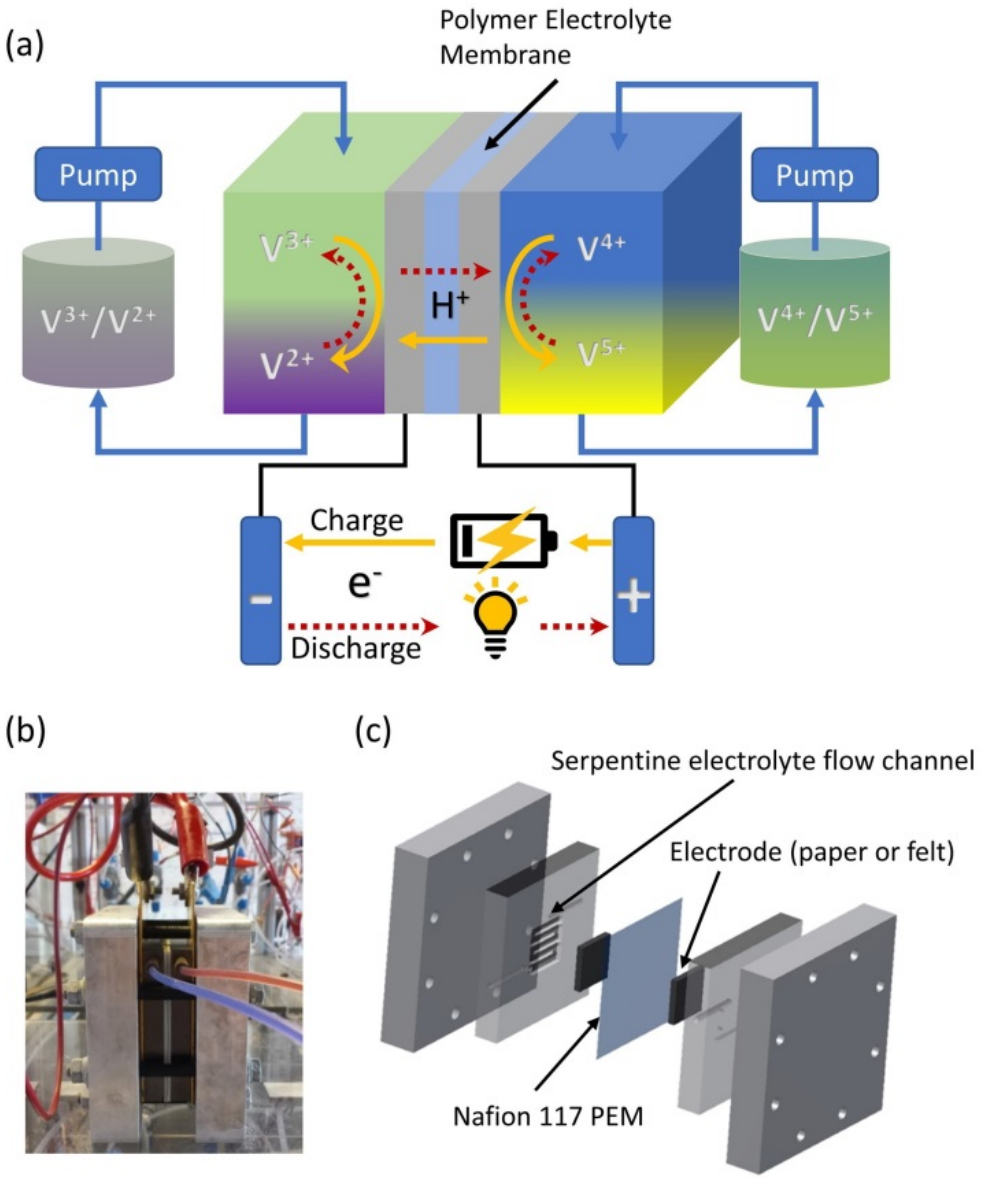

Figure 15. (a) General schematic of a VRFB; (b) photograph showing endplates, graphite flow fields, and electrolyte tubing; (c) schematic showing layers in VRFB (not shown are polytetrafluoroethylene (PTFE) gaskets).

2. VRFB electrodes and carbon materials

Greater electrode activity is accomplished by two broad modification schemes, each with their own advantages and limitations. Electrode activity can be improved by *functionalizing* the electrode surfaces in various atmospheres, often at elevated temperature, or chemical baths with the benefit of increasing surface area and/or catalytic activity. The second modification scheme is based on *surface deposition* of catalytic, nanoscale particles to achieve the same goals. Metal and metal oxide particles have been added to carbon electrodes to act as catalytic sites, with some observed improvement over pristine electrodes [53-56]. However, the propensity for these catalytic particles to decay must be thoroughly investigated. In addition to improved electrochemical activity, electrode treatments can also improve surface area, leading to greater kinetic activity solely by virtue of more reaction sites (as opposed to, or in addition to, sites with greater activity). Increased surface area can arise from thermal treatments [48] and chemical treatments [57] without including significant changes in the chemical makeup of electrode materials. Addition of carbon-based material also increases surface area, similar to the effects of etching and oxidizing treatments. Ideally, such carbon materials will have sufficiently high specific surface area to significantly improve overall electrode surface area with relatively little mass compared to the supporting electrode. The specific surface area for typical carbon paper or carbon felt has been measured in the range of 1 - 10 m^2/g [48, 58]; thus, most modified electrodes use these materials as a support or as the sole electrode material. Graphene, with its one-atom thick structure, has a maximum specific surface area

of 2630 m^2/g [59], far greater than the electrodes typically used in VRFBs. Pristine graphene, despite its superior thermal, electrical, and mechanical properties, is often synthesized in a bottom-up, costly chemical vapor deposition (CVD) process [60]. Another form of graphene, reduced graphene oxide (rGO), is considered to be more economical and mass-producible, while retaining high specific surface area and fairly comparable electrical conductivity. The top-down Hummers method [61], which chemically oxidizes bulk graphite, mechanically exfoliates the bulk graphene oxide (GO) and then chemically reduces the oxygen binding from GO, enables this material to be significantly lower in cost than free-standing pristine graphene.

Carbon materials in different forms have been used in conjunction with carbon felt or paper electrodes in numerous studies via multiple attachment methods to improve electrode surface area [62-65]. Thermally reduced GO itself was used for the positive electrodes of VRFBs to enhance electrochemical performance [66, 67]. However, these modifications were primarily incorporated during electrode production. An alternative to those modifications has been reported only once to the authors' knowledge: Goulet et al. showed performance improvement in their laminar-flow, microfluidic VRFB via deposition of carbon nanotubes in the porous electrodes [68]. In this approach, a small amount of carbon nanotubes entered the microfluidic cells with the electrolyte and were trapped on the electrodes.

3. Scope of the present work

The work reported here focuses on addition of three classes of nanoscale carbon materials to common, porous electrodes in a conventional VRFB: (1) pristine graphene, (2) rGO flakes with nominal 280 nm diameter and 460 m^2/g specific surface area, and (3) XC-72R carbon nanoparticles of approximately 50 nm and 250 m^2/g specific surface area [69] (Table 1). The porous structures of both paper and felt electrodes were unable to hold pristine graphene of extremely thin single-atom thickness (0.335 nm).

However, a several-micron thick layer of vacuum-filtered rGO film on the paper electrode showed notable kinetic performance improvement. Passive deposition of rGO flakes and carbon nanoparticles also improved VRFB kinetic performance. Furthermore, such passive deposition can be applied to any system as a retrofit with ease. The difference in specific surface area between carbon nanoparticles and common electrodes (1 - 10 m^2/g) should enable even small additions to radically increase electrode surface area in RFBs. Finally, these particles inherently have electrochemical durability in RFBs similar to the electrodes already used in systems expected to last more than the DOE benchmark of 5,000 cycles [42]. Tradeoff between kinetic enhancement and mass transport limitation by diverse modes of addition of carbon nanomaterials to VRFB electrodes was also observed.

Table 1. Test conditions for both (a) the carbon paper electrode and (b) the carbon felt electrode with different combinations of carbon nanoparticles; (1) single or a few layers of pristine CVD graphene, (2) layer of vacuum-filtered reduced graphene oxide (rGO) film, (3) passive deposition of circulating XC-72R carbon nanoparticles, and (4) of circulating rGO flakes. The weight% of the added carbon material is based on the mass of the paper (30 mg) or felt electrode (104 mg), and the current density (mA/cm²) corresponds to the 80% voltage efficiency.

	(a) Carbon paper electrode (30 mg) 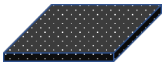	(b) Carbon felt electrode (104 mg) 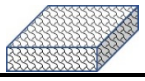
(1) Pristine CVD graphene 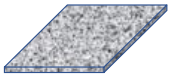	Pristine graphene destroyed by electrolyte convection (0.0005 wt%)	Unable to support pristine graphene
(2) Vacuum-filtered rGO film 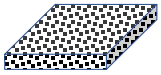	***VFRB performance improvement*** **(20 wt%, 166 mA/cm²)**	Poor contact between the electrode and the rGO film
(3) Passive deposit of suspended XC-72R 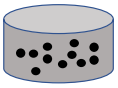	Clogged with XC-72R nanoparticles	***VFRB performance improvement*** **(10 wt%, 163 mA/cm²)**
(4) Passive deposit of suspended rGO flakes 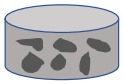	Clogged with rGO flakes	***VFRB performance improvement*** **(10 wt%, 133 mA/cm²)**

III. **Experimental**

All VRFB measurements were conducted on a 5 cm^2 flow battery with serpentine flow fields (Figure 15-b and c). Carbon paper electrodes (10AA, SGL Group) were nominally 400 μm thick before assembly, with a mass of approximately 30 mg each, and assembled with close contact between all components to minimize ohmic and mass transport losses [70]. Carbon felt electrodes (GFD3, SGL Group) were also used and had an initial mass of approximately 104 mg each. The electrolyte was 1.0 M vanadium in 5.0 M sulfuric acid, flowing at 4 mL/min-cm^2 via a peristaltic pump (Cole-Parmer). Nitrogen gas was continuously purged through both reservoirs to prevent oxygen infiltration. A Nafion 117 (DuPont) polymer electrolyte membrane (PEM) was used as the separator after pretreatment consisting of hour-long immersions in 90 °C water, then in 90 °C 0.5 M sulfuric acid, and finally immersion in 90 °C water. The VRFB was initially charged at 1.8 V with 50 mL electrolyte in the negative reservoir and 100 mL electrolyte in the positive reservoir. When the charging current fell below 4 mA/cm^2, the battery was considered fully charged, resulting in a stable open circuit voltage (OCV) exceeding 1.70 V. Following attainment of full charge, half of the positive electrolyte volume was removed, resulting in a battery with a near-100% state of charge (SOC) and 50 mL on each side. Both electrolyte reservoirs and the VRFB were maintained at 30 °C.

1. Growth of pristine graphene using CVD and its transfer onto carbon paper electrodes

Pristine graphene was grown on a 35-μm thick copper foil (Graphene Platform Corp.) via CVD resulting in a layer of 0.335 nm nominal thickness, which was then transferred to the carbon paper electrode via PMMA stamping [60]. Repetition of this transfer process would allow multiple layers of graphene to be laid on the electrode. Transfer of such thin graphene onto the felt electrode was not possible because the coarse felt structure failed to suspend graphene.

2. rGO film-modified carbon paper electrodes

For vacuum filtration, 30 mg of rGO flakes (17% oxygen content, Graphenea Inc.) was dispersed in 150 mL of isopropyl alcohol (IPA) using a sonicator for one hour. The rGO dispersion was vacuum filtered through a mixed cellulose ester membrane filter of 4-cm diameter (Hyundai micro., LTD.). The rGO film thickness and weight thus depended on the total mass of the filtered rGO flakes. In order to increase adhesion of rGO flakes, the filtered rGO film/filter was heated on a hot plate at 50 °C for 5 minutes. The baked film/filter was then soaked in acetone to separate the rGO film from the filter by dissolving the cellulose of the filter. The separated floating rGO film was then lifted by the carbon paper electrode. The rGO film/carbon paper assembly was rinsed by acetone and IPA and then air dried. Perforated rGO films were prepared by manually puncturing holes of rGO on the carbon using sharp tweezers. Additional caution with minimal force was necessary in order not to puncture through holes on the carbon paper. About 200 holes in

square grid of 1.4 mm spacing were punctured, and each hole diameter was approximately 200 μm.

3. Passive deposition of rGO flakes and XC-72R nanoparticles onto the carbon electrodes

For passive deposition, 10 mg of Vulcan XC-72R carbon nanoparticles (Cabot Corporation) or 10 mg of rGO flakes (Graphenea Inc.) was suspended in 3 mL of deionized water and sonicated for 20 minutes. This suspension was then pipetted into the electrolyte reservoirs and allowed to circulate through the VRFB. After two days of circulation through the VRFB, the electrolyte was fully discharged, remixed, redistributed between both reservoirs, and then recharged. This remix and recharge procedure is designed to “reset” the electrolyte after the occurrence of any vanadium crossover. After fully recharging the remixed electrolyte, the VRFB was discharged coulombically to 50% SOC, OCV near 1.435 V was verified, and then polarization curves and electrochemical impedance spectroscopy (EIS) measurements were performed.

4. Polarization curve analysis

The primary cell performance characterization used in this work is the polarization curve. Despite the unique insights of polarization analysis, polarization curves are not frequently encountered in battery research; such characterization relies on the system being at a constant SOC, which is inherently not the case for a battery undergoing charge or discharge processes. However, methods have been developed that ensure an effectively constant SOC during VRFB operation, enabling insights that are impossible to obtain via common

cycling [46, 71]. The polarization curves presented in this work were achieved such that voltage efficiencies over a range of current densities could be readily determined. By alternating charging and discharging steps in the polarization curves, starting at 50% SOC, an effectively constant SOC was maintained. A check on the accuracy of this "effectively-constant SOC" assumption was made by comparing pre- and post-analysis OCV, which were always within 5 mV of each other. Additionally, the voltage efficiencies reported are representative of voltage efficiencies identified via cycling since the voltage during the charge or discharge cycling step is approximated by the operating voltage at 50% SOC.

In all polarization curve results shown here, the time steps were 30 s at each current density; cell voltage was averaged over the final 15 s of each step to avoid inclusion of capacitive charging current. The voltage has been iR-corrected to remove the losses associated with electronic and ionic conductivity in the battery; this increases focus on electrode kinetic and mass transport behavior. Notes are made on polarization curves that indicate the voltages during discharge and charge that yield 80% voltage efficiency; maximum current density at the 80% voltage efficiency mark is thus the metric used to show the effects of nanoparticle deposition on VRFB performance.

5. Electrochemical impedance spectroscopy

All EIS measurements were potentiostatically controlled with a magnitude of 10 mV, spanning a frequency range from 50 kHz to 1 Hz, at open circuit. The high frequency resistance was converted to area specific resistance (ASR) after multiplying its value by the active area of the cell. Due to the practical difficulty of

performing low frequency EIS, mass transport impedance behavior was not measured.

IV. **Results and discussion**

1. Pristine graphene layer on the electrode

Notable kinetic improvements over the plain carbon paper electrodes (Figure 16-a) were not realized by placing single-layer, pristine graphene films on them (Figure 16-b). The Raman spectrum (Figure 16-c) confirms the pristine quality of the CVD graphene showing the distinctive G peak and 2D peak at 1550 cm^{-1} and 2700 cm^{-1}, respectively. Also, the Raman D peak (1350 cm^{-1}) and G peak (1550 cm^{-1}) of the carbon paper electrode show clear composition of carbon materials. The rGO film's spectrum shows relatively high I_D/I_G ratio due to its higher graphitic domains than that of carbon paper [72]. However, the tested graphene layer had a mass below 0.15 μg, which proved insufficient to significantly increase the available surface area. Additionally, the graphene layer was structurally weak and unable to remain intact in the presence of electrolyte convection by and through its fibrous structure, as shown in Figure 16-b. While the carbon paper electrode is composed of carbon fibers of 9 μm average diameter mixed with carbon flakes, the carbon felt electrode is made of similar carbon fibers but in less packing density and no carbon flakes. Despite repeated efforts, pristine graphene layers were unable to span the relatively large gaps between the fibers of the felt electrode and mostly fell apart, thus failing to allow for any reliable experiments.

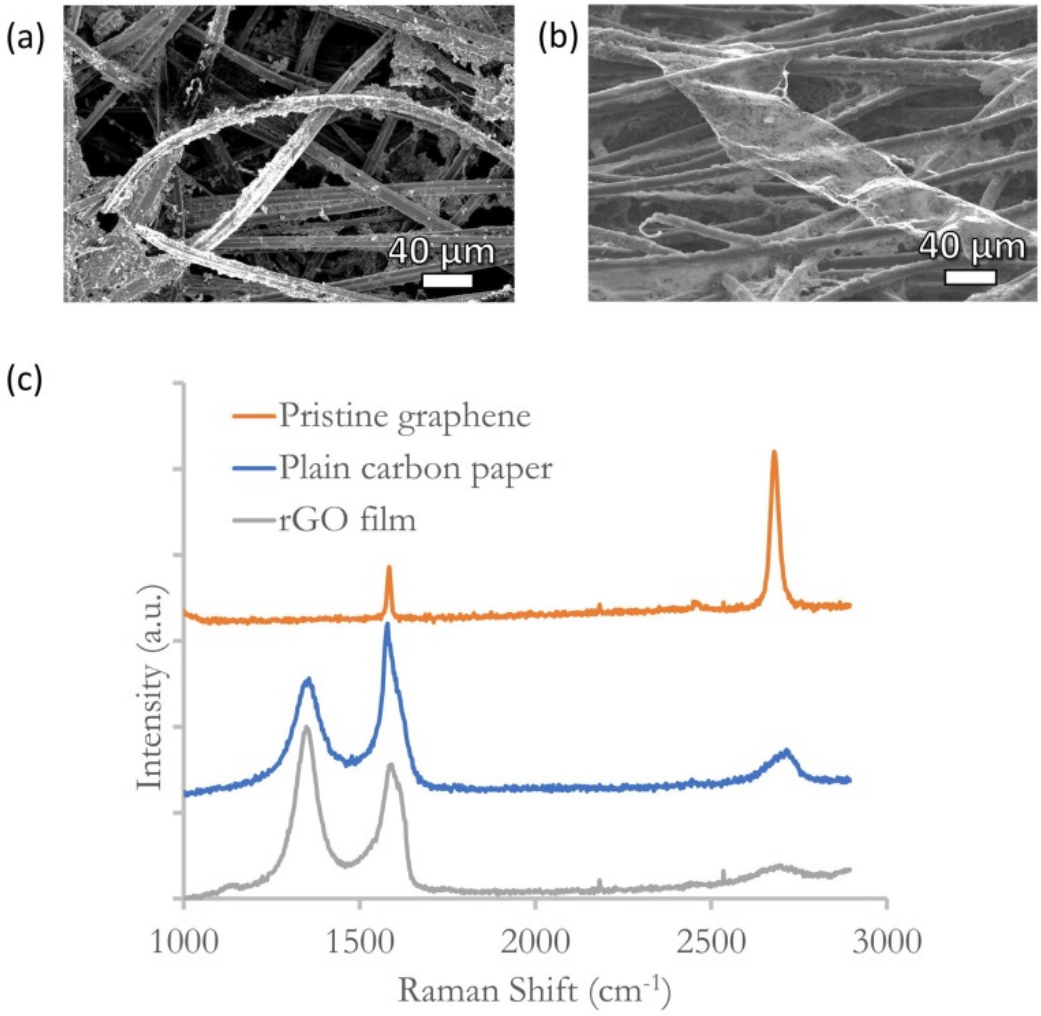

Figure 16. SEM images of (a) the original carbon paper electrode and (b) the electrode with pristine graphene supported across the paper. The SEM images were digitally optimized to improve the brightness and contrast. (c) shows Raman spectra of pristine graphene, plain carbon paper, and rGO film.

2. Vacuum-filtered rGO film on the electrodes

When a vacuum-filtered rGO film of 10 wt% of the paper electrode (Figure 17-a and b) was attached onto the PEM sides of the positive and negative paper electrodes, modest improvements to the kinetic behavior of the VRFB were observed. Addition of such a film to carbon felt electrodes failed due to its insufficient contact areas to the coarse, lower-density nature of carbon felt fibers as opposed to the more densely-packed fibers in carbon paper. Despite the relatively smaller specific surface area and slightly lower electronic conductivity of rGO compared to pristine CVD graphene, the tested rGO film with mass of approximately 10% of the supporting electrode mass showed fairly good improvement to kinetic behavior (Figure 17-c). The current density associated with 80% voltage efficiency increased from 91.0 mA/cm^2 for the plain carbon paper electrode to 101 mA/cm^2 for the rGO film laid on the electrode. While the kinetic performance was slightly improved for the rGO-film-modified carbon paper, it is clear from the polarization curve that mass transport was significantly inhibited at high current density, since the densely-packed rGO flakes allowed little mass transport through the rGO film. This tradeoff is evident from the rapid rise in overvoltage with increasing current density above 150 mA/cm^2 for the rGO film.

A greater loading of 20 wt% rGO film (Figure 18-a) was attached onto the carbon paper electrode on one side in a manner identical to that used for the above 10 wt% rGO film. Figure 18-b shows the same rGO film after having been physically perforated to improve mass transport and open up more accessible surface area. When the thick rGO film was placed on the flow field side of the electrode, the

polarization curve of Figure 18-c showed extreme mass transport limitation restricting the current density to 37 mA/cm^2 for 80% voltage efficiency (▽), which is significantly lower than that for the plain paper electrode (■). This poor performance is mainly attributed to the denser rGO film that blocked most mass transport into the porous carbon electrode. The flow field side of the electrode has been shown to support a large fraction of redox reactions [73]; thus, the rGO film was initially placed for testing here to exploit the relatively high concentration of vanadium. Unfortunately, mass transport into the electrodes was impacted too severely.

On the other hand, when the rGO film was placed on the PEM side of the electrode, the current density associated with 80% voltage efficiency increased substantially from 131 mA/cm^2 for the plain paper electrode to 154 mA/cm^2 for the rGO film on the PEM side (●). The increase in current density at this voltage efficiency was further improved to 166 mA/cm^2 for an rGO film of identical initial mass, but one which had been physically perforated to open up macro-sized holes in the film (▲). The perforated rGO film was never placed on the flow field side of the electrode since this was expected to result in an intermediate inhibition of mass transport into the electrode. In both of the previous cases with rGO film on the PEM side of the electrode, with or without holes, clear kinetic gains were realized over the plain paper electrode. However, as current density increased beyond the current density associated with 80% voltage efficiency, mass transport overpotential began dominating and the voltage deviated compared to that of

carbon paper. Thus, while kinetic gains were clearly made via addition of the vacuum-filtered rGO film on the PEM side of the electrodes, mass transport limitation occurred limiting the operating range of the modified system. This is one important insight of polarization curve analysis that cannot be made as readily via charge-discharge cycling analysis.

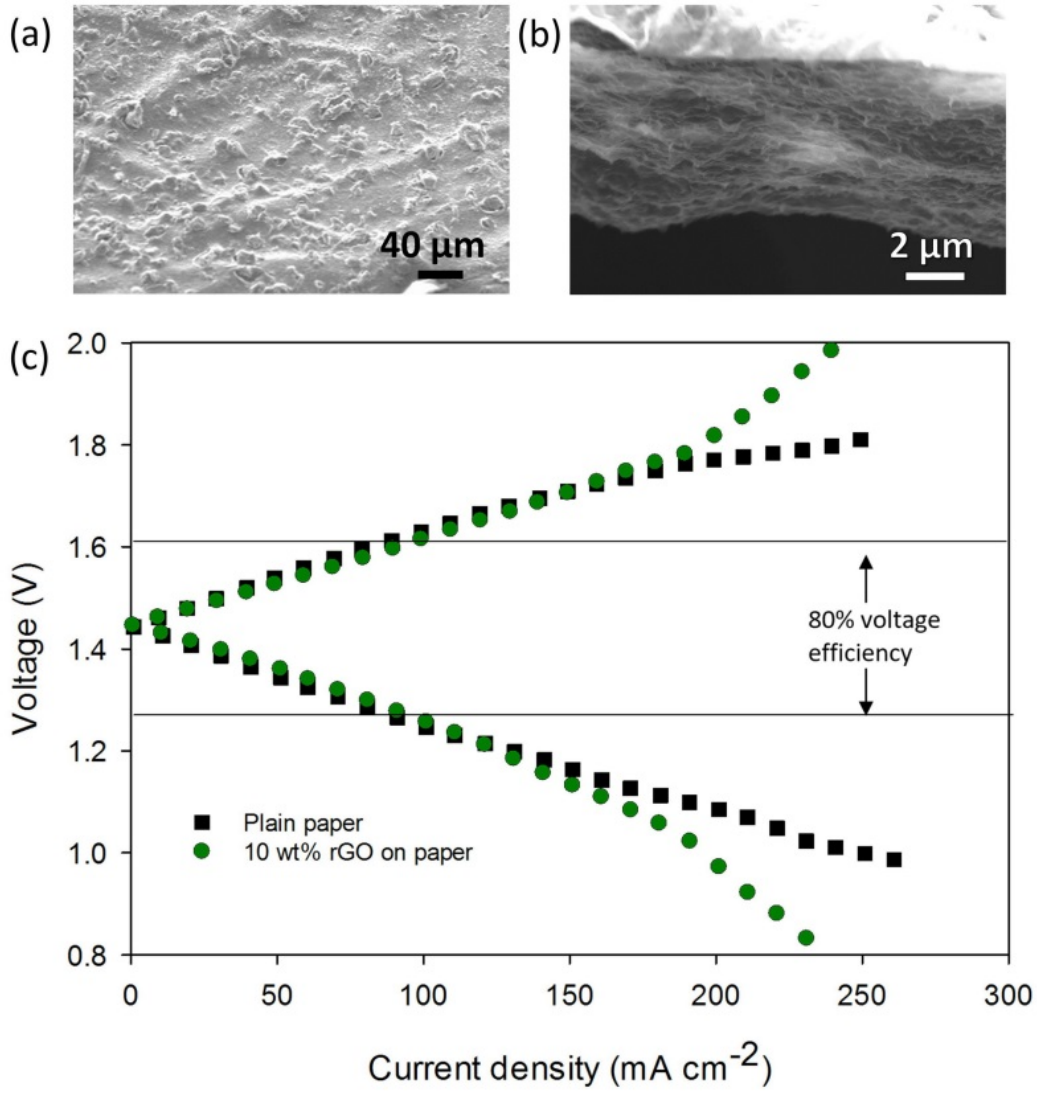

Figure 17. SEM images show 10 wt% vacuum-filtered rGO on carbon paper via (a) a face view and (b) cross-section. (c) Polarization curves showing slight kinetic improvement for rGO film added to paper along with inhibited mass transport.

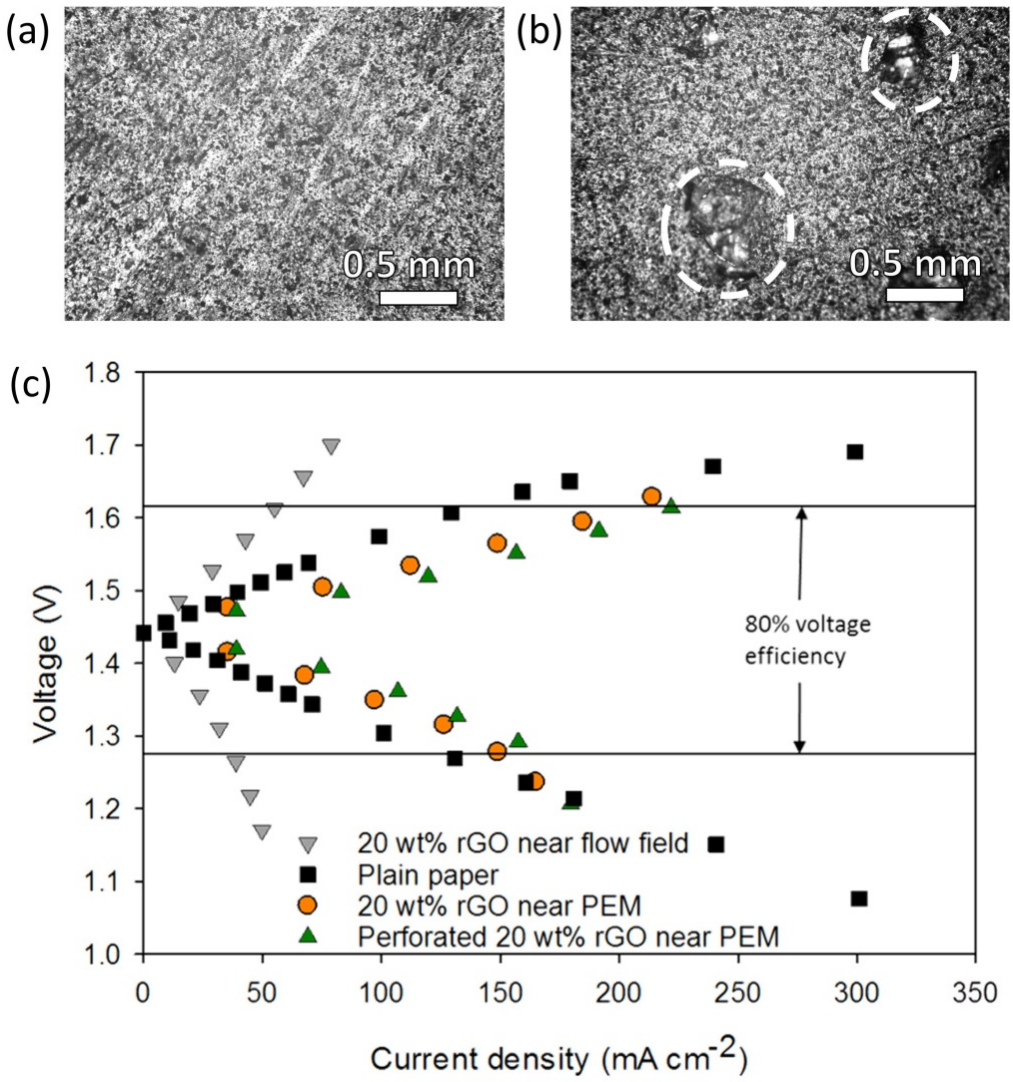

Figure 18. Optical microscope images of (a) 20 wt% rGO film on carbon paper and (b) perforated 20 wt% rGO film on carbon paper; white dashed circles indicate holes of the rGO film. (c) Polarization curve comparison showing results for 20 wt% rGO films on either side of the electrode and plain carbon paper.

3. Passive deposition of XC-72R nanoparticles or rGO flakes on the electrode

As an alternative method to increase the electrode surface area, passive deposition of either Vulcan XC-72R nanoparticles or rGO nano-flakes was performed; the loading of nanoparticles suspended in electrolyte corresponded to 10 wt% of the supporting electrode. Passive deposition results are only shown for carbon felt electrodes because the more densely-packed carbon paper electrode fibers clogged with addition of both type of nanomaterials. The clogging in the paper was likely due to a combination of its more densely-woven fiber structure and the carbon flakes already present (see Figure 16-a). Passive deposition experiments were thus possible only with the less dense felt electrode made of relatively loosely woven carbon fibers of 9 μm diameter with no flakes between fibers (Figure 19-a). Raman spectra (Figure 19-b) for both new and used felt electrodes show identical locations of D (1350 cm^{-1}), G (1600 cm^{-1}) and 2D (2700 cm^{-1}) peaks, and their similar peak intensities demonstrate their high-quality carbon materials. XC-72R nanoparticles, however, do not show any sign of 2D peak primarily because of the dominating amorphous carbon structures [74]. Because the Raman spectra of XC-72R and pristine carbon felt have common D (~1350 cm^{-1}) and G (~1600 cm^{-1}) peaks, XC-72R deposited electrodes show no discernable Raman peaks from the pristine carbon felts.

Figure 19-c and d show the negative and the positive carbon felt electrodes, respectively, after passive deposition and testing of the XC-72R suspension; the deposited XC-72R nanoparticles on carbon felt fibers are clearly observable.

Addition of both XC-72R nanoparticles and rGO nano-flakes increased the current density associated with 80% voltage efficiency (Figure 19-e): 53.1 mA/cm^2 for plain carbon felt, to 133 mA/cm^2 for the rGO flakes on felt (●), and up to 161 mA/cm^2 for the XC-72R addition (▼). It is noted that the passive deposition of nanoparticles was conducted on the felt electrodes that were first used to obtain the plain electrode results. In addition, since the electrolyte was remixed and recharged to erase the effect of vanadium crossover during the two days of passive deposition, the observed increases in current density were due solely to the addition of nanoparticles.

An interesting observation in Figure 19-e is that there is a substantial difference between rGO-deposited felt and XC-72R-deposited felt above 170 mA/cm^2, which is approximately equal to the current density corresponding to 80% voltage efficiency. While both yielded greatly improved current density up to the 80% voltage efficiency point compared to plain felt, the XC-72R addition appears to more severely impact mass transport at a higher current density. Indeed, above 200 mA/cm^2, the rGO-deposited electrode exhibited lower overvoltage, indicating better performance. This result indicates that the extent of deposition, or possibly the locations of deposited nanoparticles, can depend on the morphology of the nanoparticles circulated in suspension through the cell. The rGO is flake-like in shape while XC-72R particles are much more spherical. Further work in this direction would disentangle the extent of deposition, the particular behavior of the supporting electrode-nanoparticle composite material, and ultimately lead to the ideal loading of nanoparticles for an expected operating point. This optimal

loading depends on the current density range anticipated for a system. For reference, at 200 mA/cm^2, the voltage efficiency for XC-72R-deposited electrodes was 74% while it was 78% for the rGO-deposited electrodes. This voltage efficiency difference is not very large, but it would likely become more extreme at higher current, as indicated by the markedly different polarization curve slopes between the two systems. This behavior has strong implications on the capacity of a flow battery system to operate at higher power density if necessary under dynamic load conditions.

When comparing polarization curves in Figure 18 and Figure 19, it can be seen that carbon felt with 10 wt% rGO or XC-72R reached the same current density of approximately 170 mA/cm^2 at the 80% voltage efficiency point as 20 wt% rGO-film-modified carbon paper. In previous works, our group has shown that carbon paper tends to perform better kinetically than carbon felt, but its lower porosity inhibits mass transport [75]. Kinetic overpotential was largely alleviated in the carbon felt electrode with 10 wt% loading of nanoparticles; for reference, similar performance was observed when the rGO film was added to carbon paper, but with 20 wt% loading. An additional benefit over carbon paper, in the case of rGO-modified felt, is that the felt seemed to maintain its superior mass transport behavior, enabling more efficient operation at higher power density when needed. Furthermore, the passive addition of nanomaterials, either XC-72R or rGO flakes, allows for easy retrofit of practically any VRFB system with carbon felt electrodes.

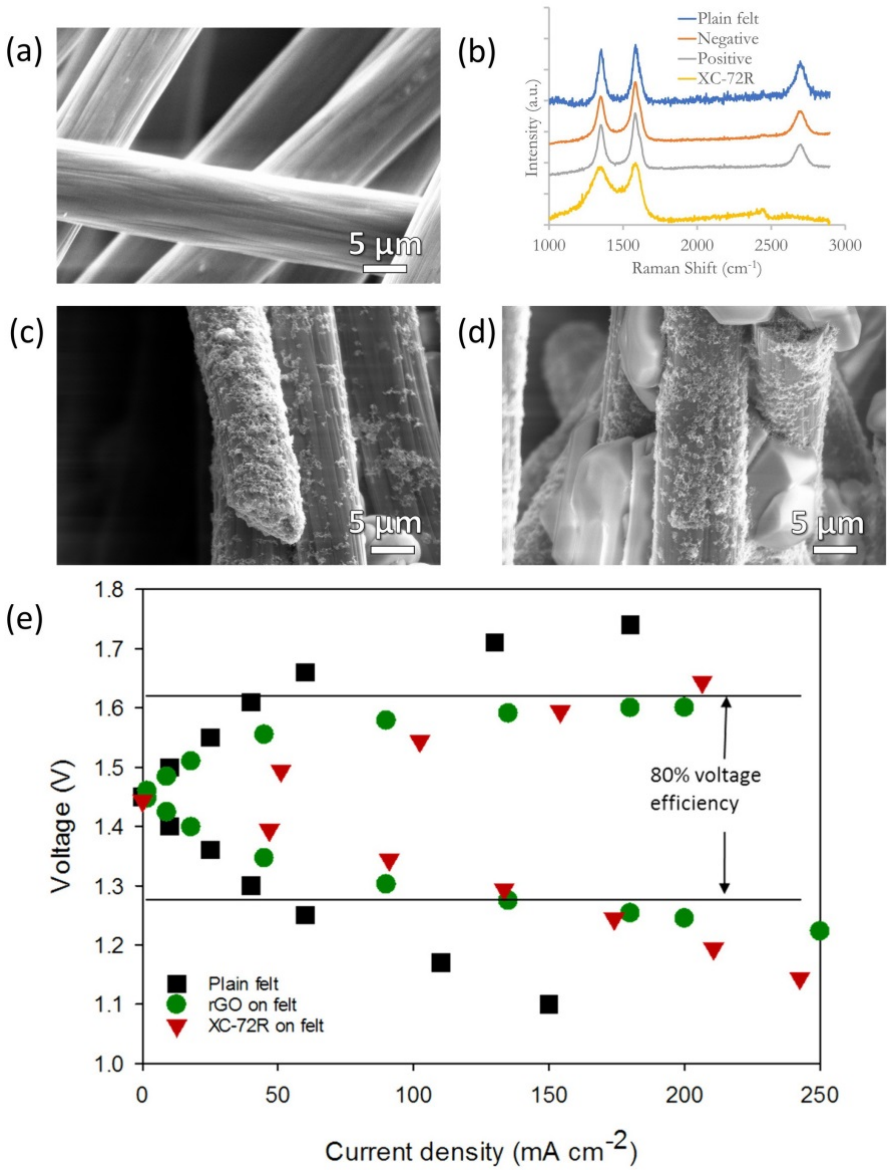

Figure 19. (a) SEM of plain carbon felt. (b) Raman spectra of plain carbon felt, negative and positive electrodes after operation in the VRFB, and XC-72R. SEMs also show XC-72R deposit on the (c) negative and (d) positive electrodes. (e) Polarization curves for plain carbon felt and after passive deposition of up to 10 wt% rGO or XC-72R.

4. Electrochemical impedance spectroscopy of the VRFB performance

In addition to polarization curves, electrochemical impedance spectroscopy (EIS) was employed to measure changes to kinetic and ohmic behavior in the VRFB. The nature of this diagnostic technique enables ready insight into phenomena that occur relatively rapidly; in this work, charge conduction (defining ohmic losses) and charge transfer (a function of electrochemical kinetics) both occur rapidly enough that no special measures were required to obtain qualitatively interpretable spectra. Mass transport behavior can be measured via EIS, but requires extra equipment to obtain stable behavior at low frequency [76]; with the present emphasis on kinetic behavior, mass transport behavior was characterized solely via polarization curves. Further evidence of the kinetic improvement by the deposition of rGO and XC-72R can be seen in Figure 20, where the high frequency charge transfer loop significantly decreased in diameter compared to that of plain felt electrodes. For raw carbon felt, this diameter was greater than 6 Ω-cm^2 while addition of 10 wt% rGO brought the diameter down to 1.7 Ω-cm^2 and the XC-72R addition yielded a diameter of 0.22 Ω-cm^2. For reference, the same charge transfer loop for perforated 20 wt% rGO film on carbon paper is also included in Figure 20

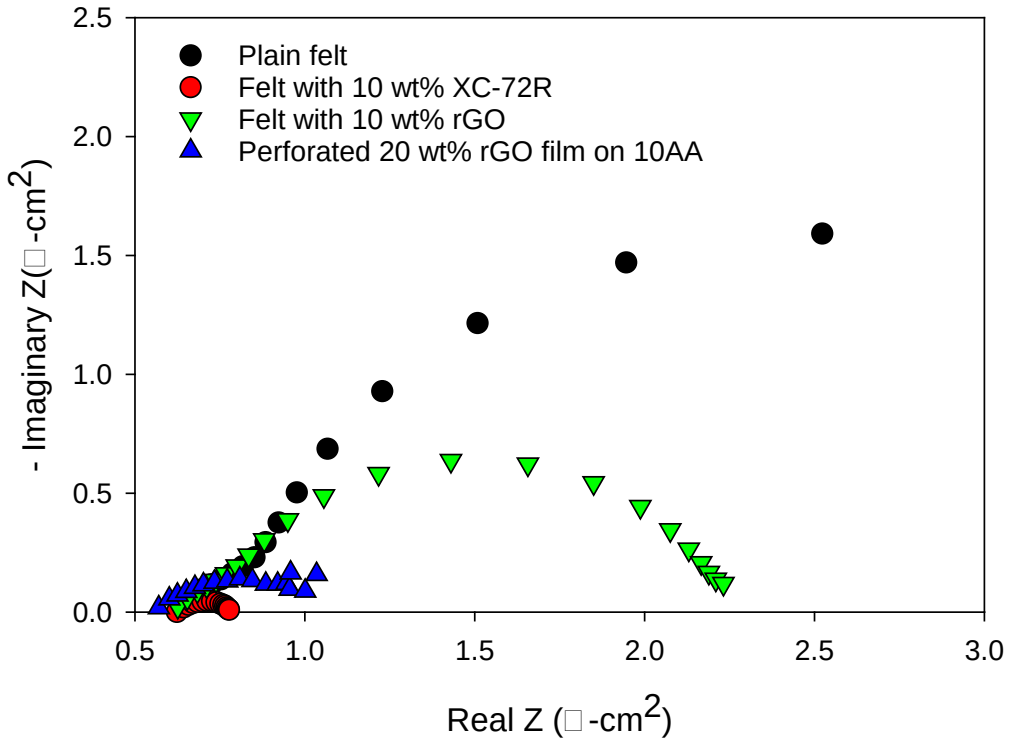

Figure 20. High frequency impedance loops indicating reduced charge transfer resistance for carbon felt electrodes after passive deposition of up to 10 wt% rGO or XC-72R nanoparticles. Impedance spectrum for 10 AA carbon paper with 20 wt% perforated rGO film is included for reference.

and shows a diameter of 0.43 Ω-cm^2. Qualitatively, this kinetic improvement is especially apparent in Figure 20, with the slopes of the polarization results becoming less steep in the 0 - 150 mA/cm^2 range. The ohmic resistance in the VRFB was unaffected by the addition of rGO or XC-72R, evidenced by near-identical high frequency intercepts for all systems; this high frequency resistance is dominated by cell compression and membrane conductivity, both of which are unaffected by the addition of nanoparticles. Further study, with extra precautions for accurate EIS measurements at low frequency, would allow for the investigation of influences on mass transport resistance arising from nanoparticle deposition on the electrodes.

The authors also note that particles clearly remained suspended in the electrolyte and adhered to the walls of the tubing after measurements were performed. From an economic perspective, it may be desirable that all particles attach to the electrodes and contribute to improved performance; thus, an optimization investigating the benefits of maintaining some fraction of particles in suspension (e.g. to counteract any electrode oxidation) compared to complete utilization of all particles by having complete deposition should be the subject of a scale-up investigation.

V. **Conclusions**

One avenue to improve cost in VRFBs is to improve power density while maintaining acceptable efficiency. By adding modest amounts of high surface area,

conductive nanomaterials to conventional electrodes, large increases in efficient power density can be realized. In this work, plain carbon paper and felt yielded current densities of 91.0 and 53.1 mA/cm^2, respectively, while remaining above 80% voltage efficiency. However, carbon paper with 20 wt% rGO in a film reached 166 mA/cm^2; carbon felt with 10 wt% rGO reached 133 mA/cm^2 and 10 wt% XC-72R carbon nanoparticles reached 163 mA/cm^2 while maintaining 80% voltage efficiency. In all of these cases, the electrode modifications are expected to be durable since both rGO and XC-72R are highly carbonized materials, chemically similar to the supporting electrode materials. Results from the nanoparticle additions indicate significant potential to refine the balance between improved kinetics and reduced electrode porosity, suggesting that a much greater efficient current density is possible. Furthermore, nanoparticle addition to the felt electrodes was demonstrated via passive deposition. This scheme allows such additions to be performed on currently-deployed RFBs or on new systems to realize immediate improvements in system efficiency. Significantly improved electrochemical kinetics were demonstrated with modest negative impact on mass transport characteristics. Further optimization of particle properties and loading amount is expected to yield kinetic enhancement while alleviating the negative impact on mass transport. A better understanding of how the nanoparticles remain physically attached to the electrodes, as well as identification of any non-uniform deposition, would be of great interest to guide further development of these electrode modifications. Finally, such modifications should be made on

intermediate-scale stack systems prior to attempted adoption in industrial-scale VRFBs to investigate scale-up considerations as well as inform economic analysis.

Acknowledgments

This work was mainly supported by the Volkswagen USA Corp. (Grant R011370023) and partially supported by the University of Tennessee equipment funding for the Raman spectroscopy system (Grant R011371077). K.D. Kihm expresses special thanks to H.G. Kim and W.M. Lee of Seoul National University for their help in preparing for vacuum-filtered rGO film samples and acknowledges the support of the Nano-Material Technology Development Program (R2011-003-2009) through the National Research Foundation of Korea (NRF) funded by the Ministry of Science, ICT and Future Planning.

Chapter 5
Conclusions

Since graphene was popularized in 2004, more than 17000 graphene-related papers and 9000 patents have been published as of 2016 [77]. Despite graphene's popularity, however, it is still hard to find popularized commercial products utilizing graphene. I expect this dissertation to be a contribution to paving a way for popularizing graphene applications.

Graphene quantum dot is fluorescent under UV light because of its nanometer-scale size, and its fluorescence is quenched when it forms a complex with mercury ions. Because the GQD quenching effect has high selectivity towards mercury ions [23], the GQD has been proposed as a mercury sensing probe. Because there have been demands for portable mercury ion quantification devices due to serious toxicity of mercury ions, we decided to utilize GQD in inventing facile mercury ion quantification methods.

We could successfully find a facile way to reliably quantify the mercury ion concentration by measuring quenched brightness of dried GQD coated filter paper disks in flat sample wells. The most difficult hurdle during development was to obtain a consistent quenched brightness at one mercury ion concentration. The consistency could be drastically increased by inventing a simple step, making good contact between a filter paper disk and the bottom surface by pressing the disk.

The brightness of the fluorescent disk was measured by digitally processing microscopic images via a python script. Our finally invented method may require only a UV light source, a brightness sensor, a microcomputer, and a tiny sample holder where GQD coated filter paper disks are located, and it will greatly increase the portability of a future-developed device.

The lowest mercury ion detection limit of the method which we could reach using filter paper was around 0.5 ppm, and it was mainly because of the inherent fluorescence of the filter paper. Thus, we tried to use translucent silica gel as a GQD container to lower the detection limit further by removing background fluorescence. We could successfully synthesize silica-gels and make dried fluorescent GQD-contained silica-gels. However, we needed more time to resolve an important problem: keeping GQDs inside silica-gels while allowing mercury ions to reach the GQDs inside of the silica-gels. Although there seems to remain a long way to utilize silica gels in mercury ion quantification, this chapter may be a beginning point by suggesting the idea.

Reduced graphene oxide is another type of graphene material, which is synthesized by chemically exfoliating graphite flakes. Because rGO flakes are relatively larger than GQD, they could be made into a porous film via vacuum-filtration. So, when such an electrically conductive porous film is used in modifying carbon electrodes, the surface area of the electrode is expected to increase.

Vanadium redox flow battery has various advantages as grid-scale energy storage, but its cost is still high to be widely used. As an effort to reduce the cost,

we tried to enhance the battery's performance by modifying its carbon electrodes using carbon nano-particles such as reduced graphene oxide and xc-72 carbon nano-particles. We chose two different strategies in maximizing the current density of the battery by increasing the number of reaction sites in the electrodes: attaching vacuum-filtered rGO film to the carbon electrodes and passively depositing carbon nano-particles to the electrodes. As a result, we achieved up to 26 % (carbon paper, 131 to 166 mA/cm^2) enhancement for the first method, and up to 200 % (carbon felt, 53.1 to 161 mA/cm^2) enhancement for the second method.

To sum up, among various graphene materials, we could successfully utilize graphene quantum dots and reduced graphene oxide in two different applications. Graphene opened up new 2D-material science fields, and various 2-D materials also have been discovered. In the future, other 2-D materials may be used to enhance the performance of our applications further.

List of References

1. Novoselov, K.S., et al., *Electric Field Effect in Atomically Thin Carbon Films.* Science, 2004. **306**(5696): p. 666.
2. Bolotin, K.I., et al., *Ultrahigh electron mobility in suspended graphene.* Solid State Communications, 2008. **146**(9): p. 351-355.
3. Balandin, A.A., et al., *Superior Thermal Conductivity of Single-Layer Graphene.* Nano Letters, 2008. **8**(3): p. 902-907.
4. Lee, C., et al., *Measurement of the Elastic Properties and Intrinsic Strength of Monolayer Graphene.* Science, 2008. **321**(5887): p. 385.
5. Zhao, H.-L., X. Zhu, and Y. Sui, *THE SHORT-LIVED CHINESE EMPERORS.* 2006. **54**(8): p. 1295-1296.
6. *Laws and Resolutions.* [cited 2019 09/04]; Available from: https://noharm-uscanada.org/issues/us-canada/laws-and-resolutions#regional.
7. Davidson, P.W., G.J. Myers, and B. Weiss, *Mercury Exposure and Child Development Outcomes.* Pediatrics, 2004. **113**(Supplement 3): p. 1023.
8. *Minamata Disease The History and Measures - Chapter 2*. 2002; Available from: http://www.env.go.jp/en/chemi/hs/minamata2002/ch2.html.
9. 石原, 信., *情報無視が続いた水俣病原因解明の歴史.* 日本衛生学雑誌, 2014. **69**(1): p. 75-79.
10. Bernhoft, R.A., *Mercury toxicity and treatment: a review of the literature.* Journal of environmental and public health, 2012. **2012**: p. 460508-460508.

11. Fernandes Azevedo, B., et al., *Toxic effects of mercury on the cardiovascular and central nervous systems.* Journal of biomedicine & biotechnology, 2012. **2012**: p. 949048-949048.

12. Zhu, M., et al., *Ultrasensitive detection of mercury with a novel one-step signal amplified lateral flow strip based on gold nanoparticle-labeled ssDNA recognition and enhancement probes.* Biosensors and Bioelectronics, 2014. **61**: p. 14-20.

13. Nikolaos, K.-K. and F. Spyros, *Recent Advances in the Analysis of Mercury in Water - Review*. Current Analytical Chemistry, 2016. **12**(1): p. 22-36.

14. Suvarapu, L.N. and S.-O. Baek, *Recent Studies on the Speciation and Determination of Mercury in Different Environmental Matrices Using Various Analytical Techniques.* International Journal of Analytical Chemistry, 2017. **2017**: p. 3624015.

15. Li, L., et al., *Graphene Quantum Dots as Fluorescence Probes for Turn-off Sensing of Melamine in the Presence of Hg2+*. ACS Applied Materials & Interfaces, 2014. **6**(4): p. 2858-2864.

16. Zhu, S., et al., *Strongly green-photoluminescent graphene quantum dots for bioimaging applications.* Chemical Communications, 2011. **47**(24): p. 6858-6860.

17. Li, Y., et al., *An Electrochemical Avenue to Green-Luminescent Graphene Quantum Dots as Potential Electron-Acceptors for Photovoltaics.* Advanced Materials, 2011. **23**(6): p. 776-780.

18. Yan, X., et al., *Large, Solution-Processable Graphene Quantum Dots as Light Absorbers for Photovoltaics.* Nano Letters, 2010. **10**(5): p. 1869-1873.

19. Dutta, M., et al., *ZnO/Graphene Quantum Dot Solid-State Solar Cell.* The Journal of Physical Chemistry C, 2012. **116**(38): p. 20127-20131.

20. Wang, B., et al., *Fluorescent graphene quantum dot nanoprobes for the sensitive and selective detection of mercury ions.* Spectrochimica Acta Part A: Molecular and Biomolecular Spectroscopy, 2014. **131**: p. 384-387.

21. Chakraborti, H., et al., *Interfacing water soluble nanomaterials with fluorescence chemosensing: Graphene quantum dot to detect Hg2+ in 100% aqueous solution.* Materials Letters, 2013. **97**: p. 78-80.

22. Anh, N.T.N., A.D. Chowdhury, and R.-a. Doong, *Highly sensitive and selective detection of mercury ions using N, S-codoped graphene quantum dots and its paper strip based sensing application in wastewater.* Sensors and Actuators B: Chemical, 2017. **252**: p. 1169-1178.

23. Yan, Z., et al., *A green synthesis of highly fluorescent nitrogen-doped graphene quantum dots for the highly sensitive and selective detection of mercury(ii) ions and biothiols.* Analytical Methods, 2016. **8**(7): p. 1565-1571.

24. Bian, S., et al., *One-pot synthesis of sulfur-doped graphene quantum dots as a novel fluorescent probe for highly selective and sensitive detection of lead(ii).* RSC Advances, 2016. **6**(74): p. 69977-69983.

25. Gu, S., et al., *Sulfur and Nitrogen Co-Doped Graphene Quantum Dots as a Fluorescent Quenching Probe for Highly Sensitive Detection toward Mercury Ions.* ACS Applied Nano Materials, 2019.

26. Zhu, S., et al., *Photoluminescence mechanism in graphene quantum dots: Quantum confinement effect and surface/edge state.* Nano Today, 2017. **13**: p. 10-14.

27. *ITU Recommendation BT. 601-7.* 2011; Available from: https://www.itu.int/dms_pubrec/itu-r/rec/bt/R-REC-BT.601-7-201103-I!!PDF-E.pdf.

28. Feldman, M. and P. Desrochers, *Research Universities and Local Economic Development: Lessons from the History of the Johns Hopkins University.* Industry and Innovation, 2003. **10**(1): p. 5-24.

29. (US), P.W.A., *SILICA GEL AND PROCESS OF MAKING SAME.* WALTER A. PATRICK: United States.

30. Gurav, J.L., et al., *Silica Aerogel: Synthesis and Applications.* Journal of Nanomaterials, 2010. **2010**: p. 11.

31. *All About Nafion.* Available from: https://www.permapure.com/resources/all-about-nafion-and-faq/.

32. Shannon, R., *Revised effective ionic radii and systematic studies of interatomic distances in halides and chalcogenides.* Acta Crystallographica Section A, 1976. **32**(5): p. 751-767.

33. Aaron, D., et al., *Kinetic enhancement via passive deposition of carbon-based nanomaterials in vanadium redox flow batteries.* Journal of Power Sources, 2017. **366**: p. 241-248.

34. Perry, M.L. and A.Z. Weber, *Advanced Redox-Flow Batteries: A Perspective.* Journal of The Electrochemical Society, 2016. **163**(1): p. A5064-A5067.

35. Kundu, D., et al., *A high-capacity and long-life aqueous rechargeable zinc battery using a metal oxide intercalation cathode.* Nature Energy, 2016. **1**: p. 16119.

36. Weber, A.Z., et al., *Redox flow batteries: a review*. Journal of Applied Electrochemistry, 2011. **41**(10): p. 1137-1164.

37. de Leon, C.P., et al., *Redox flow cells for energy conversion*. Journal of Power Sources, 2006. **160**(1): p. 716-732.

38. Ha, S. and K.G. Gallagher, *Estimating the system price of redox flow batteries for grid storage.* Journal of Power Sources, 2015. **296**: p. 122-132.

39. Kear, G., A.A. Shah, and F.C. Walsh, *Development of the all-vanadium redox flow battery for energy storage: a review of technological, financial and policy aspects.* International Journal of Energy Research, 2012. **36**(11): p. 1105-1120.

40. Moore, M., et al., *Capital Cost Sensitivity Analysis of an All-Vanadium Redox-Flow Battery*. ECS Transactions, 2012. **41**(17): p. 1-19.

41. Viswanathan, V., et al., *Cost and performance model for redox flow batteries.* Journal of Power Sources, 2014. **247**: p. 1040-1051.

42. *Grid Energy Storage Dec. 2013*. 2013 2017.04.19]; Available from: https://energy.gov/oe/downloads/grid-energy-storage-december-2013.

43. Bourke, A., et al., *Electrode Kinetics of Vanadium Flow Batteries: Contrasting Responses of V-II-V-III and V-IV-V-V to Electrochemical Pretreatment of Carbon*. Journal of the Electrochemical Society, 2016. **163**(1): p. A5097-A5105.

44. Ryu, J., M. Park, and J. Cho, *Catalytic Effects of B/N-co-Doped Porous Carbon Incorporated with Ketjenblack Nanoparticles for All-Vanadium Redox Flow Batteries*. Journal of the Electrochemical Society, 2016. **163**(1): p. A5144-A5149.

45. He, Z.X., et al., *Mn3O4 anchored on carbon nanotubes as an electrode reaction catalyst of V(IV)/V(V) couple for vanadium redox flow batteries*. Electrochimica Acta, 2015. **176**: p. 1434-1440.

46. Aaron, D., et al., *In Situ Kinetics Studies in All-Vanadium Redox Flow Batteries*. ECS Electrochemistry Letters, 2013. **2**(3): p. A29-A31.

47. Houser, J., et al., *Influence of architecture and material properties on vanadium redox flow battery performance*. Journal of Power Sources, 2016. **302**: p. 369-377.

48. Pezeshki, A.M., et al., *High performance electrodes in vanadium redox flow batteries through oxygen-enriched thermal activation*. Journal of Power Sources, 2015. **294**: p. 333-338.

49. Pezeshki, A.M., et al., *Full Cell Study of Diels Alder Poly(phenylene) Anion and Cation Exchange Membranes in Vanadium Redox Flow Batteries*. Journal of the Electrochemical Society, 2016. **163**(1): p. A5154-A5162.

50. Doan, T.N.L., T.K.A. Hoang, and P. Chen, *Recent development of polymer membranes as separators for all-vanadium redox flow batteries.* RSC Advances, 2015. **5**(89): p. 72805-72815.

51. Sun, C.N., et al., *Evaluation of Diels-Alder poly(phenylene) anion exchange membranes in all-vanadium redox flow batteries.* Electrochemistry Communications, 2014. **43**: p. 63-66.

52. Aaron, D., et al., *Polarization curve analysis of all-vanadium redox flow batteries.* Journal of Applied Electrochemistry, 2011. **41**(10): p. 1175-1182.

53. Wei, L., et al., *Copper nanoparticle-deposited graphite felt electrodes for all vanadium redox flow batteries.* Applied Energy, 2016. **180**: p. 386-391.

54. Li, B., et al., *Bismuth Nanoparticle Decorating Graphite Felt as a High-Performance Electrode for an All-Vanadium Redox Flow Battery*. Nano Letters, 2013. **13**(3): p. 1330-1335.

55. Tsai, H.M., et al., *Preparation and electrochemical activities of iridium-decorated graphene as the electrode for all-vanadium redox flow batteries.* Electrochimica Acta, 2012. **77**: p. 232-236.

56. Flox, C., et al., *Active nano-CuPt3 electrocatalyst supported on graphene for enhancing reactions at the cathode in all-vanadium redox flow batteries.* Carbon, 2012. **50**(6): p. 2372-2374.

57. Zhou, X.L., et al., *A high-performance dual-scale porous electrode for vanadium redox flow batteries.* Journal of Power Sources, 2016. **325**: p. 329-336.

58. Sun, C.N., et al., *Hydrogen evolution at the negative electrode of the all-vanadium redox flow batteries.* Journal of Power Sources, 2014. **248**: p. 560-564.

59. Bonaccorso, F., et al., *Graphene, related two-dimensional crystals, and hybrid systems for energy conversion and storage.* Science, 2015. **347**(6217): p. 1246501.

60. Li, X., et al., *Large-Area Synthesis of High-Quality and Uniform Graphene Films on Copper Foils.* Science, 2009. **324**(5932): p. 1312-1314.

61. Hummers, W.S. and R.E. Offeman, *Preparation of Graphitic Oxide.* Journal of the American Chemical Society, 1958. **80**(6): p. 1339-1339.

62. González, Z., et al., *Outstanding electrochemical performance of a graphene-modified graphite felt for vanadium redox flow battery application.* Journal of Power Sources, 2017. **338**: p. 155-162.

63. Wei, G.J., et al., *A new electrocatalyst and its application method for vanadium redox flow battery.* Journal of Power Sources, 2015. **287**: p. 81-86.

64. Wei, G.J., et al., *Electrospun carbon nanofibers/electrocatalyst hybrids as asymmetric electrodes for vanadium redox flow battery.* Journal of Power Sources, 2015. **281**: p. 1-6.

65. Manahan, M.P., et al., *Carbon nanoporous layer for reaction location management and performance enhancement in all-vanadium redox flow batteries.* Journal of Power Sources, 2013. **222**: p. 498-502.

66. González, Z., et al., *Graphite oxide-based graphene materials as positive electrodes in vanadium redox flow batteries.* Journal of Power Sources, 2013. **241**: p. 349-354.

67. González, Z., et al., *Thermally reduced graphite oxide as positive electrode in Vanadium Redox Flow Batteries.* Carbon, 2012. **50**(3): p. 828-834.

68. Goulet, M.A., A. Habisch, and E. Kjeang, *In Situ Enhancement of Flow-through Porous Electrodes with Carbon Nanotubes via Flowing Deposition.* Electrochimica Acta, 2016. **206**: p. 36-44.

69. Holade, Y., et al., *Enhancing the available specific surface area of carbon supports to boost the electroactivity of nanostructured Pt catalysts.* Physical Chemistry Chemical Physics, 2014. **16**(46): p. 25609-25620.

70. Aaron, D.S., et al., *Dramatic performance gains in vanadium redox flow batteries through modified cell architecture.* Journal of Power Sources, 2012. **206**: p. 450-453.

71. Pezeshki, A.M., et al., *The Cell-in-Series Method: A Technique for Accelerated Electrode Degradation in Redox Flow Batteries.* Journal of the Electrochemical Society, 2016. **163**(1): p. A5202-A5210.

72. Sobon, G., et al., *Graphene Oxide vs. Reduced Graphene Oxide as saturable absorbers for Er-doped passively mode-locked fiber laser.* Optics Express, 2012. **20**(17): p. 19463-19473.

73. Gandomi, Y.A., et al., *In Situ Potential Distribution Measurement and Validated Model for All-Vanadium Redox Flow Battery.* Journal of the Electrochemical Society, 2016. **163**(1): p. A5188-A5201.

74. Ferrari, A.C. and D.M. Basko, *Raman spectroscopy as a versatile tool for studying the properties of graphene.* Nature Nanotechnology, 2013. **8**(4): p. 235-246.

75. Liu, Q.H., et al., *High Performance Vanadium Redox Flow Batteries with Optimized Electrode Configuration and Membrane Selection.* Journal of the Electrochemical Society, 2012. **159**(8): p. A1246-A1252.

76. Sun, C.-N., et al., *Resolving Losses at the Negative Electrode in All-Vanadium Redox Flow Batteries Using Electrochemical Impedance Spectroscopy*. Journal of the Electrochemical Society, 2014. **161**(6): p. A981-A988.

77. Zou, L., et al., *Trends Analysis of Graphene Research and Development.* 2018. **3**(1): p. 82.

Appendix

I. Design of filter paper well

OpenScad source code:

```
VR=2; VH=0.5; HT=20;
function htot(r) = VH+r*sqrt(3)+HT;

module onemold(r) {
  $fn=40;
  HTOT=htot(r);
  pointss=[ [0,0], [VR,0],
        [VR,VH+VR*sqrt(3)],
      [r,HTOT-HT], [r,HTOT], [0,HTOT] ];
   rotate_extrude()
     polygon(pointss);
}


module tile(an,bn, r, th,H) {
  rr=(r+th)*2;

  idx=0;
  for (a=[0:an-1], b=[0:bn-1]) {
      x=rr*(a+0.5)+th;
      y=rr*(b+0.5)+th;
      //cord=sqrt(x*x+y*y);
      //if (a!=-an || b!=-bn) {
      {  translate([x,y,-0.01]) {
              bth=1;
              //cylinder($fn=50,bth, r-1,r-1);
              translate([0,0,bth-0.01])
               cylinder($fn=50,H-bth+0.03, r,r);
        }
      }
  }
}

module mold(R, TH,H1) {
    unit=(R+TH)*2;
    mark=3;
    xn=4; yn=6;
        difference() {
          cube([unit*xn+TH*2,unit*yn+TH*2,H1], center=false);
          tile(xn,yn,R,TH,H1);
        }
    translate ([15,-mark*1/2,0]) rotate([0,0,30])
cylinder(H1,3,3,$fn=2);
}

module top(R,TH, H) {
    tth=0.1;
    ru=(R+TH)*2;
    cube([ru, ru*4+TH*2, 1.2]);
    translate([-TH-tth,-tth,0]) tile(1,4,R-tth,TH+tth,H);
```

```
}
//mold(0.25*25.4/2);
RR=5.8/2; TH=1;
mold(RR, TH,4.5);
translate([35,55,0]) rotate([0,0,90]) top(RR,TH,7);
```

II. Image processing script (python)

```
#!/usr/bin/env python3
'''
 * Greyscale brightness calculation from micrsocope images

 * Written by
   Sinchul Yeom (syeom@vols.utk.edu)
   Mechanical, Aerospace and Biomedical Engineering Department
   University of Tennessee, Knoxville

 Last update : 8/6/2019

'''

import glob, os, sys, re
from pathlib import Path
import time#, dateutil.parser
from datetime import date, datetime, timedelta
from PIL import Image, ImageDraw
import numpy as np
import numpy.ma as ma
from tinydb import TinyDB, Query
import struct


save_del=','
src_ext = [ '*.jpg', '*.BMP' ]
t_start=0

bmp_struct='''
typedef struct {
  char   bm[2];
  uint   fsize;
  char   rsv[4];
  uint   offset;
  uint   hdsize;
  int    width;
  int    height;
  short  cplane; // 1
  short  bpp;
  int    comp;
  uint   imsize;
  int    hres;   // ppm
  int    vres;   //ppm
  uint   ncolor;
```

```
  uint   nicolor;
} __attribute__((__packed__)) h;
'''

tgt_dir=os.path.expanduser('~')+"/knox/qdHg/"
name_pat = { 'Sample' : '^s([^_]*)_', 'Conc' : '_(\d*\.\d+|\d+)ppm',
             'Mag' : '(\d+)x', 'Gain' : '_g(\d)_', 'Exposure' :
'_e(\d+)_*',
             'Idx':'_(\d+)(_|$)', 'Ref':'_(ref)$', 'Rad':'_r(\d+)_',
             'Elap':'_(\d+)m_', 'Seq':'-(\d+)$', 'SeqTerm':'_(\d+)s_',
             'Vol' :'_W*(\d+)ul_',
        }
# 'RelW', 'RelW_std','RelG', 'RelG_std','RelR', 'RelR_std', 'RelB',
'RelB_std',

header = [
             'PPM','Seq','Sample', 'Time',
             'W',
             'B',
             'G',
             'R',
             'W_std',
             'B_std',
             'G_std',
             'R_std',
             '',
             'Sample', 'Idx', 'Seq', 'Vol', 'Conc', 'Mag', 'Gain',
'Exposure', 'Degrade', 'Elap',
            #'B/G', 'B/G_std',
             'NorG', 'NorG_std', 'NorR', 'NorR_std',  'NorB',
'NorB_std',
        ]
header_str=""
R2G=[ 0.299, 0.587, 0.114 ]
for k in header:
    header_str+=k+save_del

src_dirs= [ "/gdrive/kmicro/", "/gdrive/kmicromax/" ]
#src_dirs= [ "/gdrive/kmicro/" ]

dlist=[]
for i in src_dirs:
    root=os.path.expanduser('~')+i
    filedb=Path(root+'qdhg_db.json')
    dlst=glob.glob(root+'qdHg*/')
    dlist.extend([{ "src":i, "list":dlst,
       "db" : TinyDB(filedb)}])

gmask={}

def natural_sort_key(s, _nsre=re.compile('([0-9]+)')):
    return [int(text) if text.isdigit() else text.lower()
            for text in re.split(_nsre, s)]

def save_data(f, data):
```

```
    np.savetxt(f,
        data,
        fmt='%s',
        delimiter=save_del,
        newline='\r\n',
        header=header_str)

def add_ppm(last_dic, conc=-1):
    if 'Conc' in last_dic:
        last_dic.update( {'PPM' : last_dic['Conc'] })
    elif conc >= 0:
        last_dic.update( {'PPM' : conc })

def add_row(sdata, row):
    r=[]
    for k in header:
        v=''
        if (k in row): v=row[k]
        r.append(v)
    sdata.append(r)

def add_rows(sdata, rows):
    for r in rows: add_row(sdata, r)

def filtered_output(keyarr, records, sdata, sep=True):
    keys=set()
    key=keyarr[0]
    for row in records:
        if (key in row):
            keys.add(row[key])

    for k in sorted(keys):
        ten=list(filter(lambda el: el.get(key, None) == k, records))

        if (len(keyarr) > 1):
            filtered_output(keyarr[1:], ten, sdata, sep)
        else:
            add_rows(sdata, ten)
            if sep: sdata.append(['']*len(header))


def get_masks(box, outr, inr, mode="RGB"):
    key=str(box)+'_'+str(outr)+'_'+str(inr)
    if (key not in gmask):
        (iX, iY)=box
        xc=iX/2; yc=iY/2
        mask = Image.new(mode,box,'white')
        dr = ImageDraw.Draw(mask)
        dr.ellipse([(xc-outr,yc-outr), (xc+outr,yc+outr)],'black')
        if (inr > 0):
            dr.ellipse([(xc-inr,yc-inr),(xc+inr,yc+inr)],'white')
        #mask.save(key+".jpg")
        gmask.update({key : np.array(mask)})

    return gmask[key]
```

```
g_elap_arr=[]

def proc_exptime_flush():
    global g_elap_arr

    if (len(g_elap_arr) > 0):
        ret=[ i.get('W',None) for i in g_elap_arr]
        m_val=(max(ret))
        m_idx=ret.index(m_val)
        m_dict=g_elap_arr[m_idx]
        degrade=float(m_dict.get('Exposure'))*sum(ret)/m_val
        m_dict.update({'Degrade' : degrade})
        add_ppm(m_dict, 0)
        #print(degrade)
        #t=[ i['Time'] for i in g_elap_arr]
        #ret=[i['Time'] for i in g_elap_arr]

        #print(t)
        #for k in g_elap_arr:
        #   k.update({'Hellow' : 'Nono'})
        #print(g_elap_arr)

    g_elap_arr.clear()

def proc_exptime_add(row):
    global g_elap_arr
    #row.update({'Hellow' : 'World'})
    g_elap_arr.append(row)

def readBMP16(file, R):
    with open(file, 'rb') as f:
        chunk = f.read(54)
        h=depack_bytearray_to_dict(chunk,bmp_struct)
        #print(h)
        if (h.get("bm") != "BX"):
            print("[ERR] Not bmp file...")
        if (h.get("bpp") != 16):
            print("[ERR] Not 16 bit bmp file...")

        f.seek(h["offset"]);
        bytepp=h["bpp"]/8;
        width=h["width"]
        height=h["height"]
        #rstep=int(height*bytepp+3)//4*4;
        #print(rstep, width, height)

        fmt = "<%dH" % (width*height)
        region=np.array(struct.unpack_from(fmt,
f.read())).reshape(width,height)
        msk=get_masks((width,height),R,0,"1")
        #print(msk[500,500])
        ima=ma.masked_array(np.array(region), mask=msk)

        return({"W":ima.mean(), "W_std":ima.std()})
```

```
        #print(valid_d)

def proc_onefile(db, f,arr_dict,idx):
    global s_last, t_start, cur_conc, g_elap_arr

    sp=Path(os.path.abspath(f))
    pp=sp.parent

    if (sp.is_dir()):
        return

    sp_crop=sp.parent.joinpath(sp.stem+".jpeg")
    if (sp_crop.exists()):
        sp=sp_crop

    apath=str(sp)
    splen=80-len(apath)
    if splen < 0: splen=1
    print('  >> Processing : '+sp.name, end=' '*splen+'\r')

    cur_row={}
    for k in name_pat:
        m=re.search(name_pat[k], sp.stem)
        if (m):
            val=m.groups()[0]
            if (k == 'Conc'): val=float(val)
            cur_row.update({k : val})

    skip=False
    db_cur=None
    for r in db.search(Query().path == apath):
        #if (r.get('cyl') == cyl):
        db_cur=r
        skip=True
        break

    if not skip:
        db_cur= {'path':apath } #, 'cyl': cyl }
        if (sp.suffix == ".BMP"):
            img_average=readBMP16(sp, 500)
        else:
            img=Image.open(sp)
            outR=1500
            (xres,yres)=img.size
            xc=xres/2; yc=yres/2
            box=tuple(map(int, (xc-outR,yc-outR,xc+outR,yc+outR)))
            region = img.crop(box)
            rarr=np.array(region)
            ima=ma.masked_array(np.array(region),
mask=get_masks(region.size, outR, 0))
            #im = Image.fromarray(ima.filled(0), mode="RGB")
            #im.save("test.jpg")
            aR=ima[:,:,0];aG=ima[:,:,1];aB=ima[:,:,2]
            img_average= { 'R' : aR.mean(), 'G' : aG.mean(), 'B' :
aB.mean(), \
```

```
                        'R_std':aR.std(), 'G_std':aG.std(),
'B_std':aB.std()}

        db_cur.update({'imgval' : img_average})
        db.insert(db_cur)

        #https://www.mathworks.com/help/matlab/ref/rgb2gray.html

    db_cur_img=db_cur['imgval']
    #print(db_cur_img)
    if (not db_cur_img.get('W',False)):

w=db_cur_img['R']*R2G[0]+db_cur_img['G']*R2G[1]+db_cur_img['B']*R2G[2]

w_std=db_cur_img['R_std']*R2G[0]+db_cur_img['G_std']*R2G[1]+db_cur_img[
'B_std']*R2G[2]
        db_cur_img.update( { 'W' : w , 'W_std' : w_std } )
    #db_cur_img.update( { 'B/G' :  db_cur_img['B']/db_cur_img['G'],
'B/G_std' : db_cur_img['B_std']/db_cur_img['G_std'] } )

    t_cur=sp.stat().st_mtime
    if (idx == 0 or idx == -2):
        t_start=t_cur
        seq_start=int(cur_row.get('Seq',-1))
        #proc_exptime_add(cur_row)
        g_elap_arr=[]

    cur_row.update(db_cur_img)
    cur_row.update( {'Time' : (t_cur-t_start)/60 })

    #print(cur_row)
    g_elap_arr.append(cur_row)

    if (idx < 0):
        #print(g_elap_arr)
        ret=[ i.get('W',None) for i in g_elap_arr]
        m_val=(max(ret))
        m_idx=ret.index(m_val)
        m_dict=g_elap_arr[m_idx]
        #degrade=float(m_dict.get('Exposure'))*sum(ret)/m_val
        #m_dict.update({'Degrade' : degrade})
        add_ppm(m_dict, 0)

    arr_dict.append(cur_row)

def sortbydate(list):
    if (len(list) <= 0): return
    if (list[0].endswith('.BMP')): return
    list.sort(key=os.path.getmtime)

for slst in dlist:
    print("## Processing : "+slst.get("src"))
    db=slst.get("db")
    for sdir in slst.get("list"):
        pdir=Path(sdir)
```

```
ftgt=Path(tgt_dir).joinpath(pdir.name+'.csv')

if (ftgt.exists()):
    dmtime=os.path.getmtime(pdir)
    csv_time=ftgt.stat().st_mtime
    if (dmtime < csv_time):
        #print('  - Skipping : '+str(ftgt))
        continue

print('>>> Directory: '+pdir.name)

ddate=None
cdate=None
#ref_db=[]
cur_conc={}
cur_solute={}
dir_idx=None
cur_idx=None
m=re.search('qdHg(\d+)_', pdir.stem)
if (m): dir_idx=int(m.groups()[0])

m=re.search('[^\d](\d{8})', pdir.stem)
if (m):
    val=m.groups()[0]
    ddate=datetime.strptime(val, '%Y%m%d')

tlist = []
#s_last=-1
arr_dict=[]

#find_references(sdir, arr_dict)

for ext in src_ext: tlist.extend(glob.glob(sdir+ext))
tslist=sorted(tlist, key=natural_sort_key)

nlist=[]
lnf=""
tslist2=[]
#print(tslist)
for f in tslist:
    #print(f)
    #nf=re.sub('-\d+\.jpg','',f)
    nf=""
    m=re.search('/s([^_]*)_', f)
    if (m): nf=m.groups()[0]
    if (lnf != nf):
        if (len(nlist) > 0):
            sortbydate(nlist)
            tslist2.append(nlist)
        lnf=nf
        nlist=[]

    nlist.append(f)
```

```
        sortbydate(nlist)
        tslist2.append(nlist)

        for grp in tslist2:
            grp_len=len(grp)
            for idx in range(grp_len-1):
                proc_onefile(db, grp[idx],arr_dict,idx)

            # Last element
            iidx=-1
            if (grp_len == 1): iidx=-2
            proc_onefile(db, grp[-1],arr_dict, iidx)
            arr_dict.append({})

        #proc_exptime_flush()
        #if (len(arr_dict)>0): add_ppm(arr_dict[-1])

        sdata=[]
        #filtered_output('Elap', arr_dict, sdata)
        #filtered_output('Degrade', arr_dict, sdata, False)
        #filtered_output('PPM', arr_dict, sdata, True)
        filtered_output(['Sample', 'PPM'], arr_dict, sdata, True)
        filtered_output(['PPM', 'Sample'], arr_dict, sdata, True)
        filtered_output(['PPM'], arr_dict, sdata, True)

        add_rows(sdata,arr_dict)

        #print(arr_dict)
        print('\n  - Saving \''+ftgt.name+'\'...')
        save_data(ftgt, sdata)



######## modified from depack #########
#https://stackoverflow.com/questions/17244488/reading-struct-in-python-
from-created-struct-in-c/17244645
#https://pastebin.com/XJyZMyHX
import re
import struct
from collections import OrderedDict
from collections import namedtuple

TYPE_REGEX=re.compile("\\s*([a-zA-Z0-
9_ ]+)\\s+(\\w+)(?:\\[(\\d*)\\])?;")
#\s* -- all spaces on left from type name
#([a-zA-Z0-9_ ]+) -- type name
#\s+ -- spaces between type and name
#(\w+) -- variable name
#(?:\[(\d*)\\])? -- elements in array, optional

TYPES_DICT={"uint64_t":"Q","uint32_t":"I","uint16_t":"H","uint8_t":"B",
                "int64_t":"q","uint":"I", "int":"i","int32_t":"i",
                "int16_t":"h","int8_t":"b",
                "short":"h", "ushort":"H",
                "char":"c","bool":"?","float":"f","double":"d",
```

```
                "long long int":"q","unsigned long long int":"Q"};


def structInfo(cStruct, alignment="="):
    pack_format=alignment
    varlist=[];
    for line in cStruct.splitlines():
        #print(line)
        try:
            line=line.split("//", 1)[0].strip()
            if (not line): continue
            vartype, varname, arrayLength=TYPE_REGEX.findall(line)[0]
            vartype=TYPES_DICT.get(vartype.strip());
            if arrayLength:
                arrayLength=int(arrayLength);
            else:
                arrayLength=1;

            pack_format+=vartype*arrayLength
            varlist.append([varname,arrayLength])
        except IndexError:
            pass
    return varlist, pack_format


def depack_bytearray_to_dict(bindata, cStruct, alignment="="):
    result=OrderedDict()
    varlist,pack_format=structInfo(cStruct,alignment)
    #print(pack_format, bindata)
    unpacked=struct.unpack(pack_format,bindata)

    if pack_format[0] in '@=<>!':
        pack_format=pack_format[1:]

    ind=0;
    for varname,arrlen in varlist:
        #varname=varname.decode()
        if arrlen>1:
            if pack_format[ind]=="c":
                result[varname]=str(
                    u''.join([i.decode() for i in
unpacked[ind:ind+arrlen]]))
            else:
                result[varname]=unpacked[ind:ind+arrlen]
            ind+=arrlen
        else:
            result[varname]=unpacked[ind]
            ind+=1
    return result

######## modified from depack #########
```

III. Silica hydrogel mold design

OpenScad source code:

```
//https://www.desmos.com/calculator/m8piefutxg
function elfunc(x) = A*pow(x,8)+B*x*x;
function steps( start, no_steps, end) = [start:(end-start)/(no_steps-
1):end];
function flatten(l) = [ for (a = l) for (b = a) b ] ;
function elh(r)=r/(P3-P1)*(elfunc(P3)-elfunc(P2));
maxs=15;
A=0.6; B=0.5;

//P1=(-A-sqrt(A*A-3*B))/3;
//P2=(-A+sqrt(A*A-3*B))/3;
P1=0;
P2=0;
P3=1.17;

pointe=[for (a=steps(P1,maxs,P3)) [ a,elfunc(a)]];
points=flatten([ pointe, [[P3,elfunc(P3)], [P1,elfunc(P3)]]]);

module onemold(RR) {
$fn=40;
rotate_extrude()
  scale([RR/(P3-P1), RR/(P3-P1),0]) translate( [-P1,-elfunc(P2),0])
#polygon(points);
}

circlefn=20;
module container(OD, th, bth, h) {
    OR=OD/2;
    $fn=circlefn;
    IR=OR-th;
    cylinder(bth,OR,OR);
    translate([0,0,bth]) difference() {
        cylinder(h-0.01,OR,OR);
        cylinder(h,IR,IR);
    }
}

module hexagon_tile(OD, r, th) {
  OR=OD/2;
  an=round(OR*0.7/r); bn=round(OR*2/sqrt(3)/r);
  for (a=[-an:an], b=[-bn:bn]) {
      x=r*sqrt(3)*a;
      y=-a*r+2*r*b;
      cord=sqrt(x*x+y*y);
      if (cord <= OR*1.2) {
          translate([x,y,0]) onemold(r-th);
      }
  }
}
```

```
module pillar_sub(h1,R1, R2) {
    $fn=10;
    IR=R2-1;
    sphere(R1);
    cylinder(h1,IR,IR);
}


//outD=44;

pilD=3;
conH1=8;
conH2=4;//conH1-pilD;
botTH=2;

cutTop=5;
module mold(outD, R) {
    TH=0.5;
    H1=elh(R-TH)-0.01;
    echo(H1);
    difference() {
      union() {
        difference() {
          cylinder($fn=circlefn,H1,outD/2,outD/2);
          hexagon_tile(outD,R,0.3);
        }
        translate ([0,0,-botTH]) container(outD, 1, botTH,
max(H1,conH1));
        cylinder($fn=circlefn,conH2,pilD,pilD);
       }

      union() {
      translate ([0,0,-botTH]) pillar_sub(H1*2,pilD, pilD);
      translate ([0,0,H1-cutTop]) cylinder(cutTop+1,outD,outD);
      }

    }
}


//mold(44,7);
//mold(44,4.7);
mold(38, 6);
//mold(61,6);
```

Vita

Sinchul was born in Seoul, South Korea. In 1998, he graduated Hansung Science high school which was established by Government of South Korea to raise science, technology, engineering, and mathematics (STEM) specialized students. He earned his B.S. degree in Materials Science and Engineering from Seoul National University, South Korea in 2005. During his undergraduate, he worked at Unidata Communication Systems, Inc. as an alternative for the mandatory military enlistment in South Korea for about four years as a software team leader. He went to United States in 2005 and received M.S. degree in Materials Science and Engineering from University of California, Los Angeles in 2006. He earned his Engineer's degree in Materials Science from California Institute of Technology in 2015.